J Mater Sci: Mater Electron (2026) 37:694

Tunable dielectric properties and impedance spectroscopy analysis of Au/PVA:($CoFe_2O_4$–rGO)/n–Si structures over a wide frequency and voltage range

Gülçin Ersöz Demir[1,*], Seçkin Altındal Yerişkin[2], Kevser Yıldız[3], Yashar Azizian Kalandaragh[4,5,6], and Ahmet Demir[7,8]

[1] *Faculty of Business Administration, Department of Management Information Systems, Düzce University, Düzce, Turkey*
[2] *Department of Chemistry and Chemical Processing Technologies, Vocational School of Technical Sciences, Gazi University, Ankara, Turkey*
[3] *Department of Advanced Technologies, Graduate School of Natural and Applied Sciences, Gazi University, Ankara, Turkey*
[4] *Faculty of Applied Sciences, Department of Photonics, Gazi University, Ankara, Türkiye*
[5] *Photonics Application and Research Center, Gazi University, Ankara, Türkiye*
[6] *Faculty of Basic Sciences, Department of Physics, University of Mohaghegh Ardabili, Ardabil, Iran*
[7] *Faculty of Science, Department of Physics, Düzce University, Düzce, Türkiye*
[8] *Fibrobeton Inc., İstanbul 34810, Türkiye*

Received: 4 December 2025
Accepted: 23 March 2026

© The Author(s), 2026

ABSTRACT

This study comprehensively examines voltage/frequency-dependent complex dielectric (ε^*) behaviors, electric-modulus (M^*), ac conductivity (σ_{ac}), Nyquist-diagram in the Au/PVA:($CoFe_2O_4$–rGO)/n–Si structures by using impedance spectroscopy (IS) measurements in the wide-range (0.3 kHz–3 MHz) and voltage (− 2.0 V/ + 3.0 V). Through a comprehensive dielectric-voltage-frequency analysis, three distinct operational regions are identified: (i) the reverse bias region (− 2.0 V ≤ V ≤ − 0.4 V) shows notably low and frequency-independent real dielectric (ε') below 30, indicative of limited-charge carrier dynamics within extended depletion layers; (ii) the depletion region (− 0.4 V ≤ V ≤ + 0.4 V) stabilizes ε' between 10 and 15, providing a consistent baseline for semiconductor parameter extraction; and (iii) the forward bias region (0.0 V ≤ V ≤ 3.0 V) reveals an extraordinary dielectric enhancement, with ε' reaching 140 at 0.3 kHz, attributed to interface trap (N_{it}) charging and orientational polarization of $CoFe_2O_4$ nanoparticles. A characteristic dielectric relaxation at 3.0 kHz produces bell-shaped imaginary-dielectric (ε'') peaks alongside a significant loss tangent (tanδ) of 140 at 0 V. Analysis of the real/imaginary electrical modulus (M′, M″) indicates distributed relaxation processes dominated by Maxwell–Wagner (MW) interfacial polarization, with peak M″ values between 0.28 and 0.30 under strong forward bias. AC

Address correspondence to E-mail: gulcinersozdemir@duzce.edu.tr

https://doi.org/10.1007/s10854-026-17078-2
Published online: 03 April 2026

conductivity (σ_{ac}) exhibits a substantial exponential increase, attaining 0.09 S/m at 3 MHz representing nearly a two-order magnitude rise. Impedance-spectra reveal a systematic transition from capacitance-dominated behavior (~ 17 kΩ) to a compressed resistive response (< 1 kΩ). The voltage-tunable dielectric properties of the interlayer, governed by bias-dependent charge injection and N_{it} activation, highlight its remarkable potential for next-generation adaptive electronic-devices requiring dynamic dielectric modulation.

1 Introduction

The persistent quest for improved materials with specifically engineered characteristics is fundamental to contemporary electronics, particularly for applications that require dynamic responses. Nanocomposite materials, which integrate distinct phases at the nanoscale, have thus emerged as crucial components in this field. Their capacity to exhibit synergistic properties, often significantly surpassing those of their individual constituents, renders them highly attractive for next-generation devices [1, 2]. Within this domain, composites combining metal-oxides with carbon-nanomaterials offer a compelling platform, owing to their exceptional electrical, optical, and magnetic properties, which find utility in diverse areas such as electronic-charges or energy-storage capacity, catalysis, and sophisticated electronic systems, and even with an environmentally friendly approach for energy harvesting [3–5]. Additionally, Metal–semiconductor (MS) with/without an interlayer (MIS) structures constitute fundamental building blocks in contemporary electronic device architectures, exhibiting frequency-dependent dielectric characteristics that significantly influence their operational performance [6–9]. The integration of polymeric interfacial layers between metallic contacts and semiconductor substrates has emerged as a strategic approach for modulating electrical transport properties and enhancing device reliability [10, 11]. Poly(vinyl alcohol) (PVA), a biocompatible and environmentally stable polymer, demonstrates exceptional film-forming capabilities and tunable dielectric properties, making it particularly suitable for electronic applications [12, 13]. Against this backdrop, cobalt ferrite ($CoFe_2O_4$) nanoparticles distinguish themselves as a prominent magnetic material. Their inherent attributes, including high coercivity, moderate saturation magnetization, and remarkable chemical stability, position them as particularly appealing for a wide array of technological applications [14, 15].

Recent advances in $CoFe_2O_4$ nanostructure synthesis have enabled precise control over morphology and crystallinity, significantly impacting their physical properties. Methods such as sol–gel, co-precipitation, hydrothermal, and thermal decomposition have been employed to tailor particle size, shape, and crystallinity. For example, copper doping via sol–gel produces spherical $CoFe_2O_4$ nanocrystals with sizes below 10 nm and a cubic spinel structure confirmed by XRD and Rietveld refinement [16]. Calcination temperature strongly influences crystallite size (12–123 nm) and particle morphology (84–139 nm), with higher temperatures improving crystallinity and magnetic properties in co-precipitated samples [17]. Morphology-controlled synthesis through thermal decomposition yields well-defined shapes like spheres, cubes, and hexagons, with distinct cation distributions affecting optical band gaps and magnetic behavior [18–20]. High-resolution TEM studies confirm single-crystalline nature with well-resolved lattice fringes, while substitutional doping (e.g., Eu^{3+}, Y^{3+}) can reduce particle size below 5 nm and modify magnetic states from ferromagnetic to superparamagnetic [21–23]. Overall, synthesis optimization allows tuning of $CoFe_2O_4$ nanostructures' size, shape, crystallinity, and cation distribution to enhance their structural, optical, and magnetic properties for diverse applications [1, 16, 24, 25]. $NiFe_2O_4$/rGO composites show higher saturation magnetization (~ 50 emu/g) compared to $CoFe_2O_4$ (~ 40 emu/g), reflecting the strong magnetic nature of $NiFe_2O_4$ within the spinel ferrite family MFe_2O_4 (M = Ni, Mn, Zn, Cu) [23, 26]. However, dielectric tunability in $NiFe_2O_4$/rGO composites is reported to be lower (ε' ~ 85 at 1 kHz) than typical $CoFe_2O_4$ systems under similar bias conditions, indicating differences in dielectric response despite magnetic advantages [27]. The electronic structure of $NiFe_2O_4$ reveals spin gapless ferromagnetic behavior with zero band gap at the Fermi level, contrasting with $CoFe_2O_4$'s half-metallic ferromagnetism and a direct band gap of 0.713 eV, which may influence their dielectric and magnetic

properties [26]. Spinel ferrites exhibit tunable electromagnetic properties depending on the M-site cation, with high-entropy variants showing enhanced dielectric loss and magnetic loss due to synergistic effects and hopping mechanisms [28]. Structural factors such as cation distribution and inversion degree also affect magnetic saturation and coercivity, with $NiFe_2O_4$ typically forming an inverse spinel structure that contributes to its distinct magnetic behavior [23]. Overall, while $NiFe_2O_4$ offers higher magnetization, $CoFe_2O_4$ tends to have superior dielectric tunability under comparable conditions, highlighting trade-offs within the spinel ferrite family for multifunctional applications.

The incorporation of magnetic nanocomposites, specifically $CoFe_2O_4$ nanoparticles combined with reduced graphene oxide (rGO), into polymeric matrices represents an innovative methodology for achieving enhanced dielectric performance [29, 30]. Additionally, Schottky diodes or heterostructures (SDs) especially those using 2D materials and engineered interfaces offer a promising route to electronic components with dynamically tunable properties, building on the inherent advantages of SDs such as fast switching and low forward voltage drop [31–33]. However, the performance and overall efficiency of these devices are intrinsically linked to the characteristics of the M/S interface. Here, factors such as the density and distribution of Nit play a pivotal role in modulating key electrical parameters, including ideality factor (n), barrier height (BH), and series resistance (R_s) [34–36]. The deliberate introduction of nanocomposite interlayers at these critical interfaces has been demonstrated to significantly modify the electrical behavior of SDs, thereby improving device performance and enabling novel functionalities through the effective modulation of interface trap distributions [37–39]. $CoFe_2O_4$ exhibits superior magnetic properties with high saturation magnetization and chemical stability, while rGO contributes exceptional electrical conductivity and mechanical reinforcement [40, 41]. The synergistic combination of these nanomaterials within PVA matrices creates multifunctional nanocomposites with tailored electromagnetic properties suitable for advanced electronic device applications [30, 42]. On the other hand, polarization phenomena in dielectric materials are among the most basic and vital properties of organic and inorganic compounds that fundamentally govern their frequency-dependent electrical behavior and can be systematically categorized into four primary mechanisms: electronic, ionic, dipole (orientational), and space-charge polarization (SCPs) [43–45]. Electronic-polarization manifests through electron cloud displacement relative to atomic nuclei under applied electric fields, predominantly occurring at elevated frequency ranges [46, 47]. Ionic-polarization involves the relative displacement of ionic species within crystalline lattices, demonstrating optimal response characteristics at intermediate frequency domains [48, 49]. Dipole-polarization encompasses the reorientation of permanent molecular dipole moments in response to external electric fields [45, 50, 51], exhibiting enhanced activity under reduced temperature conditions [52]. The SCPs represent a macroscopic phenomenon attributed to the heterogeneous distribution of mobile charge carriers throughout the material matrix [53], demonstrating predominant activity within low-frequency regions and elevated temperature environments [54, 55]. Maxwell–Wagner polarization constitutes a specialized manifestation of space-charge polarization, arising from charge carrier accumulation at interfaces between phases exhibiting disparate electrical conductivities [54, 56]. This interfacial polarization mechanism aligns with the theoretical framework established by Koop's theory, whereby charge carrier mobility becomes restricted, resulting in preferential charge accumulation within interfacial regions.

The existence of an insulator interfacial layer with low-dielectric, interface states (N_{ss}), barrier-inhomogeneities between metal and semiconductor, and series resistance (R_s) may cause significant deviations from the ideal situation and limits the device's performance. But the use of high-dielectric nanocomposites instead of conventional insulators grown by traditional methods, by neutralizing most unwanted interface traps, it can reduce both the leakage current and series resistance (R_s) of the device, as well as increase its electronic-charges or energy-storage capacity [10, 18, 24, 25]. Such high-dielectric interfacial layer not only obstacles an inter-diffusion between semiconductor and metal but also regulates charge transport mechanisms. On the other hand, electrical or dielectric measurements performed only within a single or narrow range of frequency, temperature, and voltage cannot provide us with sufficiently accurate and reliable results regarding either the calculated parameters or the conduction mechanisms. The performing measurements over a wide range can provide us with far more reliable results on possible conduction mechanisms. Existing works on the ferrite-polymer composites are found to

focus on either frequency-dependent permittivity at fixed voltage or voltage-dependent permittivity at single frequencies, limiting comprehensive understanding. Reports on $CoFe_2O_4$–rGO in MIM configurations show ε' values between 45 and 85 at 1 kHz but data beyond ± 1 V are lacking. Interface trap effects cannot be separated from electrode polarization in symmetric MIM geometries. Studies on metal–semiconductor structures with ferrite interlayers are scarce and critical low-frequency regimes where Maxwell–Wagner relaxation and orientational polarization dominate are often missed. The novelty: controlled trap states for voltage-tunable dielectric response are created by embedding $CoFe_2O_4$ nanoparticles in a partially reduced graphene oxide matrix, which has not been fully demonstrated experimentally. Complex permittivity, modulus, and impedance are measured across wide bias (− 2 V to + 3 V) and frequency (300 Hz to 3 MHz) ranges to distinguish competing polarization mechanisms [57–59].

This study aims to address the critical knowledge gap by providing a systematic and in-depth investigation into the frequency/voltage dependence of dielectric properties of the fabricated Au/PVA:($CoFe_2O_4$–rGO)/n–Si structures. Through the application of IS across a broad range of frequency (0.3 kHz–3 MHz) and voltage (− 2.0 V/ + 3.0 V), the complex interplay between electronic polarization mechanisms and interfacial charge dynamics within these novel composite structures was meticulously analyzed. Research identifies three distinct operational regions, characterizes characteristic dielectric relaxation phenomena, and quantifies an order-of-magnitude dielectric tunability attributed to interface trap charging and the orientational polarization of $CoFe_2O_4$ nanoparticles. Furthermore, a significant enhancement in AC conductivity and a systematic evolution of impedance from capacitive to resistive behavior were demonstrated, which validates the potential for voltage-controlled modulation of energy storage and dissipation. By establishing precise frequency–voltage relationships, this work provides fundamental insights into interfacial trap engineering and voltage-controlled dielectric tunability, thereby offering crucial design principles for the development of adaptive electromagnetic applications that require dynamic permittivity modulation.

2 Experimental details

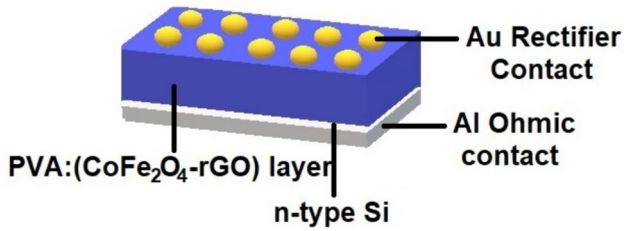
All chemical reagents were of analytical grade and obtained from Merck and Sigma-Aldrich: iron(III) nitrate nonahydrate ($Fe(NO_3)_3{\cdot}9H_2O$, ≥ 98%, Merck), cobalt(II) nitrate hexahydrate ($Co(NO_3)_2{\cdot}6H_2O$, ≥ 98%, Merck), ethylene glycol (≥ 99.5%, Merck), ammonia solution (25%, analytical grade, Merck), poly(vinyl alcohol) (PVA, Mw ~ 85,000–124,000, > 99% hydrolyzed, Sigma-Aldrich), and graphene oxide aqueous dispersion (4 mg/mL, Sigma-Aldrich). All reagents were used as received without further purification.

3 Synthesis of $CoFe_2O_4$ nanoparticles

Cobalt ferrite nanoparticles were prepared through a hydrothermal synthesis route. $Fe(NO_3)_3{\cdot}9H_2O$ (6.4 g, 15.8 mmol) and $Co(NO_3)_2.6H_2O$ (2.3 g, 7.9 mmol) were individually dissolved in ethylene glycol (40 mL each). The solutions were mixed under magnetic stirring and heated to 90 °C. A 3 M aqueous ammonia solution (50 mL) was introduced dropwise at constant temperature, producing a characteristic brown coloration indicative of precursor formation. After 20 min of continuous stirring at 90 °C, the reaction mixture was transferred to a Teflon-lined autoclave and subjected to hydrothermal treatment at 200 °C for 3 h. Following natural cooling, the black precipitate was isolated by centrifugation and purified through multiple washing cycles with deionized water and 70% ethanol until pH neutrality was achieved. The material was dried at 100 °C for 5 h.

4 Substrate preparation and metallization

The n-type Si (P-doped) wafers with (100) orientation, 2″ (5.08 cm) diameter, and 300 μm thickness were sectioned and cleaned in an ultrasonic bath by using standard RCA cleaning processes. The backside surfaces received aluminum deposition (~ 200 nm thickness) via thermal evaporation to establish ohmic contacts. Post-deposition annealing was conducted at 450 °C for 30 min under a nitrogen atmosphere to minimize contact resistance and improve metal–semiconductor adhesion.



Scheme 1 The fabricated device illustration

5 Nanocomposite film deposition

Reduced graphene oxide was incorporated into a 5 wt% polyvinyl alcohol aqueous solution at a 1 wt% concentration under stirring until complete dispersion. $CoFe_2O_4$ nanoparticles were subsequently added to the rGO-PVA matrix with continued agitation to ensure uniform distribution. The composite solution was deposited onto prepared n-Si substrates by spin coating at 2000 rpm for 40 s, followed by ambient temperature drying and thermal annealing to optimize film uniformity and substrate adhesion.

6 Schottky contact formation

Gold electrodes (1 mm diameter) were deposited through shadow mask evaporation to form rectifying contacts, completing the Au/PVA:($CoFe_2O_4$–rGO)/n–Si heterostructure fabrication. Illustration of the produced device can be seen in Scheme 1.

7 Results and discussions

Figure 1a presents the comprehensive ε'-*V*-*f* characteristics of the Au/PVA:($CoFe_2O_4$–rGO)/n–Si structures measured across the voltage range of − 2.0 V/ + 3.0 V and frequency range of 300 Hz–3 MHz. Throughout, the real dielectric constant ε' was evaluated from Eq. (1),

$$\varepsilon' = \frac{C.d}{\varepsilon_0.A} = \frac{C}{C_0} \quad (1)$$

where A is the active rectifier contact area, d is the interlayer thickness, C is the measured device capacitance, and ε_0 and C_0 denote, respectively, the permittivity of free space and the corresponding vacuum (geometrical) capacitance. The three-dimensional dielectric surface reveals distinct voltage-dependent polarization regimes governed by the interfacial electronic states and the multifunctional $CoFe_2O_4$–rGO composite interlayer. In the reverse bias region (− 2.0 V ≤ V ≤ − 0.4 V), the ε' remains below 30 across the entire frequency spectrum. The weak voltage dependence reflects the restricted charge carrier response within the extended depletion layer. Under these conditions, the wide depletion width prevents efficient interfacial charge accumulation, while deep-level traps positioned far from the Fermi level remain inactive. The independent behavior from frequency confirms that relaxation times of available polarization mechanisms significantly exceed the measurement period, resulting in minimal dielectric contribution from interface states. The depletion region (− 0.4 V ≤ V ≤ 0.4 V) exhibits dielectric convergence with ε' values stabilizing between 10 and 15 regardless of measurement frequency. This voltage-independent plateau corresponds to the depletion-dominated region where intrinsic semiconductor properties govern the dielectric response. The absence of frequency dispersion provides a reference baseline, indicating that interfacial polarization mechanisms remain energetically inaccessible and that the observed permittivity originates primarily from electronic and ionic polarization within the PVA:($CoFe_2O_4$–rGO) composite layer. The forward bias regime (0.4 V ≤ V ≤ + 3.0 V) demonstrates pronounced dielectric enhancement accompanied by systematic frequency dispersion. At 0.3 kHz, the ε' escalates to 140 at 3.0 V, representing nearly tenfold amplification relative to the depletion baseline. This substantial enhancement originates from multiple concurrent polarization mechanisms: (i) Maxwell–Wagner interfacial polarization at the PVA/n-Si heterojunction driven by conductivity mismatch between the organic and inorganic phases, (ii) orientation/dipole polarization of magnetic $CoFe_2O_4$ nanoparticles embedded within the polymer matrix under applied electric field, (iii) space-charge accumulation at the rGO/semiconductor interface facilitated by the conducting graphene network, and (iv) voltage-assisted activation of interface trap states positioned 0.2–0.4 eV below the conduction band edge. Progressive frequency stepping from 0.3 kHz to 3 MHz systematically suppresses the low-frequency dielectric enhancement as polarization mechanisms with characteristic relaxation times $\tau < 1/(2\pi f)$ become kinetically frozen. The ε' undergoes stepwise reduction, stabilizing at 80 (for 5 kHz), 40 (for 50 kHz), and 25 (for 3 MHz) at + 3.0 V. The high-frequency limiting value

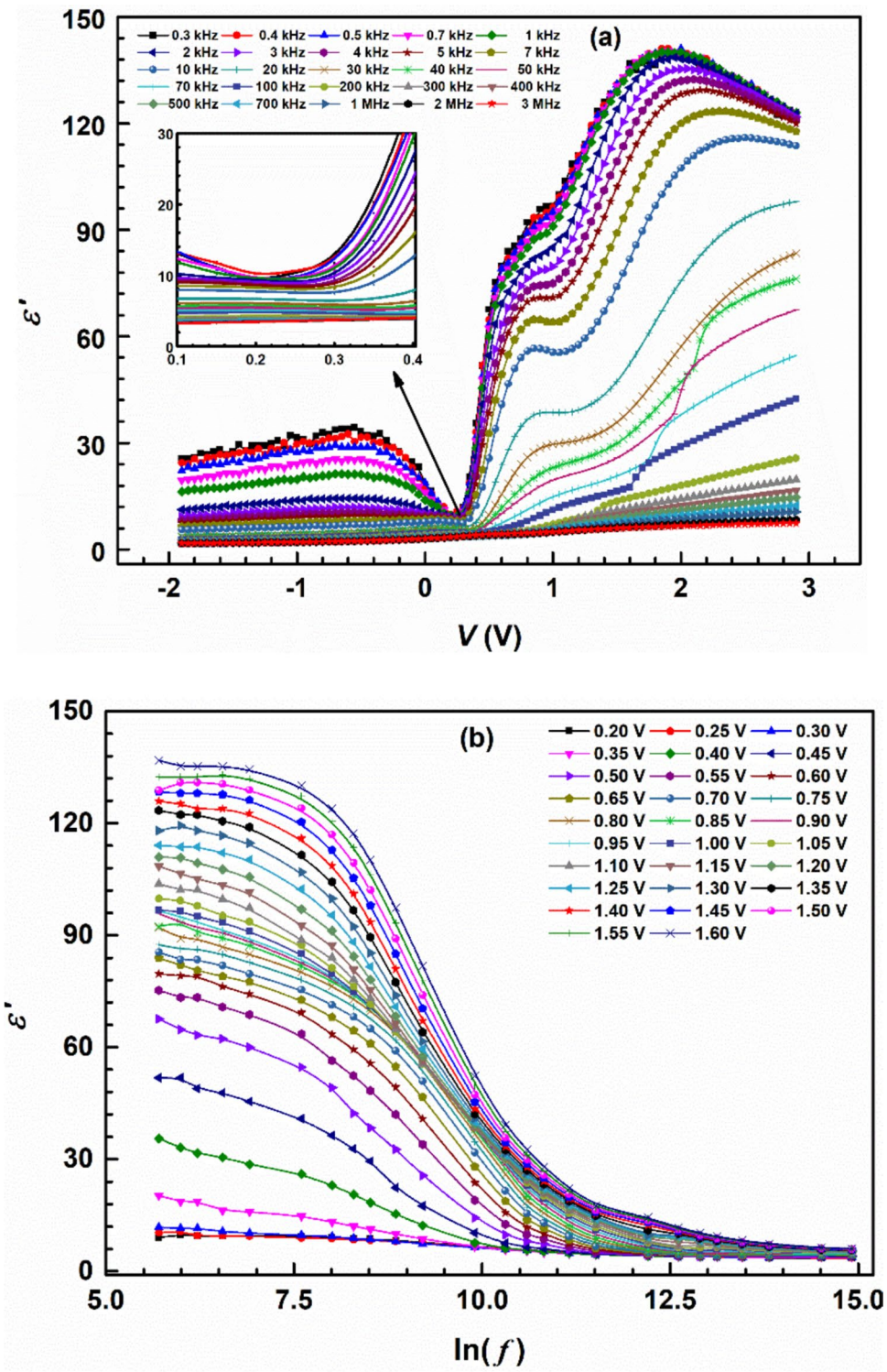


Fig. 1 **a** Frequency, and **b** voltage-dependent real dielectric permittivity (ε') of Au/PVA:($CoFe_2O_4$–rGO)/n–Si structures

represents contributions exclusively from fast electronic and distortion polarization after complete relaxation of interfacial and orientational mechanisms. The observed dielectric tunability validates the synergistic role of the $CoFe_2O_4$–rGO composite structure: the ferrimagnetic cobalt ferrite nanoparticles provide orientation polarization under alternating electrical fields. At the same time, the reduced GO network establishes

conductive pathways enabling efficient MW polarization at metal–semiconductor interfaces.

Meanwhile, Fig. 1b illustrates the voltage-dependent real dielectric permittivity (ε') as a function of frequency for the Au/PVA:($CoFe_2O_4$–rGO)/n–Si structures across DC voltages ranging from 0.20 to 1.5 V. The frequency-dependent dielectric response exhibits systematic variation with increasing bias voltage, revealing the complex interplay between electronic polarization mechanisms and interfacial charge dynamics within the composite semiconductor structure. At low frequencies ($T = 1/2\pi f > \tau$), N_{ss} with different lifetimes (τ) and a specific distribution in the semiconductor's forbidden energy gap have enough time to follow the applied AC signal, and the dipoles have enough time to rotate around itself. Thus, significant splitting occurs in the ε'–V and ε''–V curves with decreasing frequency. In other words, a significant contribution to the ε' and ε'' values occurs with decreasing frequency which is called as an excess complex dielectric. At 0.20–0.35 V, ε' holds steady at 10–20 independent of frequency; dispersion only emerges above 0.4 V, which two factors explain. First, the applied bias remains below the built-in potential (~ 0.7 V for Au/n–Si), maintaining a narrow depletion layer that prevents significant charge injection. Interface traps at 0.2–0.4 eV below the conduction band require both thermal activation and field-assisted tunneling to participate in AC polarization; at these low voltages, the band bending is insufficient (estimated field ~ 10^4 V/cm) to modulate trap occupancy on the timescale of our AC probe. Second, orientational polarization of $CoFe_2O_4$ nanoparticles necessitates overcoming magnetic anisotropy barriers ($K_1V \sim 10^{-20}$ J for 10 nm particles). The local AC field strength (~ 1 V/mm) at these biases falls below the threshold for coherent particle rotation within the measurement period. The observed $\varepsilon' \approx 15$ thus represents the intrinsic composite response, electronic polarization from PVA ($\varepsilon' \approx 3$–4) plus static contribution from immobilized ferrite inclusions (bulk $CoFe_2O_4$: $\varepsilon' \approx 12$). The frequency-flat behavior confirms no active relaxation; if traps or nanoparticles responded, dispersion would be observed as these mechanisms freeze above their characteristic frequencies. Below 0.4 V, it is measured only the passive matrix dielectric, not the voltage-activated polarization mechanisms dominating forward bias. In the 0.40–0.70 V bias range, a pronounced frequency dispersion is observed; at low frequencies, the ε' rises to ~ 30–90 and decreases monotonically with increasing frequency. This transition corresponds to the onset of interface state activation and charge injection into the PVA:($CoFe_2O_4$–rGO) interlayer, enabling enhanced polarization responses at lower frequencies where charge carriers can effectively follow the applied AC field variations. At higher bias voltages (0.75–1.50 V), the system enters the accumulation regime conditions where ε' exhibits dramatic enhancement at low frequencies, reaching maximum values of 130–140. Over the entire bias range, ε' vs. ln(f) displays an S-shaped decay with at ln(f) ~ 9–10 and converges to ~ 5–10 at a common high-frequency plateau; the breadth of this transition evidences a non-Debye response arising from a distribution of relaxation times. These trends can be rationalized by the combined effects of MW interfacial polarization at rGO/polymer boundaries, charging/discharging of interface traps, and the orientational polarization of $CoFe_2O_4$ nanoparticles. The systematic voltage dependence demonstrates that the Au/PVA:($CoFe_2O_4$–rGO)/n–Si structure functions as an actively tunable device, with its permittivity modulated by bias-controlled charge injection and interface-state dynamics. The high-frequency asymptote reflects the intrinsic dielectric response of the nanocomposite after extrinsic polarization mechanisms are effectively frozen.

Figure 2 illustrates the voltage and frequency dependence of ε'' characteristics of the studied Au/PVA:($CoFe_2O_4$–rGO)/n–Si structure across a comprehensive frequency range of 0.3 kHz–3 MHz, spanning applied voltages from − 2 V to + 3 V. The imaginary permittivity data revealed complex dielectric loss mechanisms and energy dissipation processes inherent to the composite semiconductor heterostructure. The voltage-dependent ε'' characteristics exhibited a distinctive V-shaped profile with a minimum occurring near 0 V, corresponding to the flat-band condition where dielectric losses are minimized. Under reverse bias conditions (− 2 V to − 0.5 V), the imaginary permittivity was found to demonstrate systematic frequency dependence with higher values at lower frequencies, indicating enhanced dielectric losses associated with interface state relaxation and MW-type polarization mechanisms at the rGO/Si interface.

Additionally, at moderate forward bias (0.5 to 1.5 V), the ε'' values increased substantially, particularly at lower frequencies where losses exceed 10^3 for frequencies below 1 kHz. This pronounced enhancement reflects the activation of multiple loss mechanisms, including interface trap charging/discharging

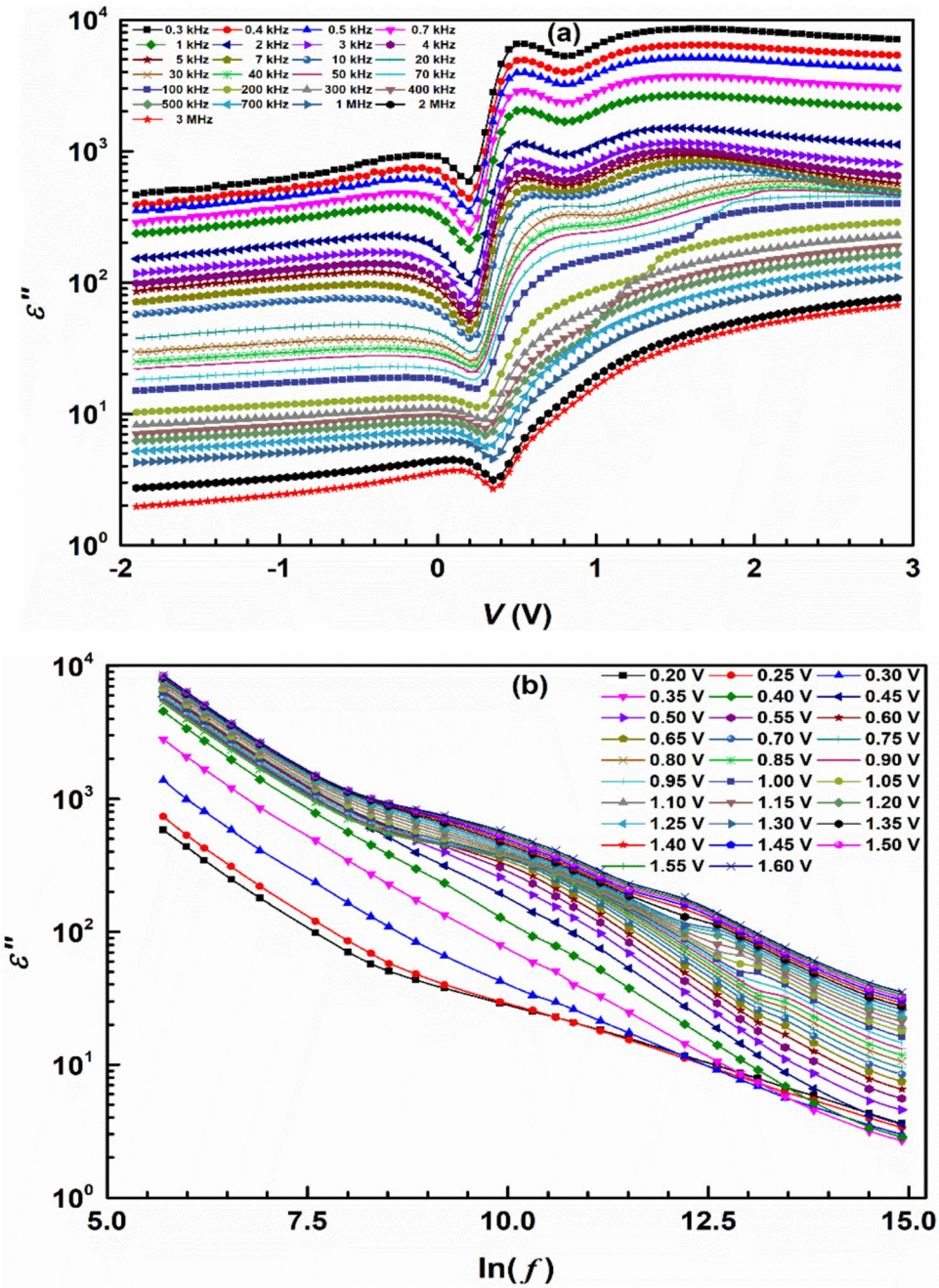


Fig. 2 **a** Frequency, and **b** voltage-dependent ε'' of Au/PVA:($CoFe_2O_4$–rGO)/n–Si structures

cycles, ionic conduction within the PVA matrix, and orientational polarization of embedded $CoFe_2O_4$ magnetic nanoparticles. The frequency-dependent decay follows approximately $1/f$ behavior, characteristic of distributed relaxation processes in heterogeneous nanocomposite systems. Under strong voltage (> 2 V), the system enters deep inversion where ε'' reaches maximum values approaching 10^4 at the lowest frequencies. This dramatic increase in dielectric losses corresponds to enhanced charge injection and accumulation at the metal–polymer interface, facilitating dc conduction processes that contribute significantly to the imaginary permittivity through the relationship from (Eq. 2)

$$\varepsilon'' = \frac{G.d}{\varepsilon_0.A.\omega} = \frac{G}{\omega.C_0} = \frac{\sigma}{\omega.\varepsilon_0} \tag{2}$$

where σ represents the ac conductivity, ω is angular frequency, and G is conductance.

The systematic frequency scaling revealed multiple relaxation areas: at frequencies below 10 kHz, interface polarization and charge injection mechanisms dominate the loss characteristics, while at frequencies above 100 kHz, the response transitions toward intrinsic dielectric losses of the composite material. The convergence of ε'' values at high frequencies (> 1 MHz) toward unity indicates that the electronic polarization mechanisms become dominant with minimal contribution from slower ionic or orientational processes. The evaluated voltage–frequency mapping demonstrates that the PVA:($CoFe_2O_4$–rGO) interlayer exhibits controllable dielectric loss characteristics through bias-dependent modulation of charge transport and polarization mechanisms. Figure 2b demonstrates the voltage-dependent ε'' as a function of frequency for the Au/PVA:($CoFe_2O_4$–rGO)/n–Si structure across applied DC voltages ranging from 0.20 to 1.50 V. The semi-logarithmic representation revealed the evolution of dielectric loss mechanisms with increasing bias voltage, providing crucial views into energy dissipation pathways within the composite semiconductor heterostructure. Based on the obtained results at low voltages (0.20–0.35 V), the imaginary permittivity was found to exhibit moderate frequency dependence with ε'' values spanning from approximately 10^3 at low frequencies to 10^1 at high frequencies. This characteristic $1/f$ decay behavior indicates the presence of distributed relaxation processes associated with residual interface states and weak polarization mechanisms within the PVA:($CoFe_2O_4$–rGO) composite layer under minimal charge injection conditions. As the applied bias is increased from 0.40 to 0.70 V, the low-frequency dielectric loss is systematically and monotonically amplified, with the ε'' reaching ~ 10^4 at lower frequencies. This amplification corresponds to the activation of additional loss mechanisms, including enhanced interface trap charging dynamics, increased ionic conduction within the polymer matrix, and the orientational polarization of $CoFe_2O_4$ magnetic nanoparticles in response to the applied electric field.

At higher voltages (0.75–1.50 V), the structure exhibits pronounced dielectric loss enhancement, particularly evident at frequencies below 10^4 Hz, where ε'' approaches 10^4. The systematic voltage-dependent increase in low-frequency losses reflects the transition into the accumulation region, where substantial charge injection occurs at the metal–polymer interface. The enhanced losses originate from increased DC conductivity contributions, as expressed through Eq. 2, where elevated ionic and electronic conduction processes dominate the dielectric response. Across all bias conditions, the decay with frequency shows a nearly bias-independent slope that follows a $1/f$ law (slope ~ − 1 on a log–log scale), indicative of MW interfacial polarization governed by a broad distribution of charge-relaxation times. The convergence of ε'' values at high frequencies (> 10^6 Hz) toward 10^1 indicates the transition to intrinsic dielectric losses of the composite material, where electronic polarization mechanisms dominate with minimal contribution from slower ionic or orientational processes. The comprehensive voltage–frequency mapping establishes that the PVA:($CoFe_2O_4$–rGO) interlayer functions as a voltage-tunable device loss medium, with controllable energy dissipation characteristics spanning three orders of magnitude. The systematic bias-dependent modulation of dielectric losses provides fundamental understanding of charge transport mechanisms and establishes operational parameters for applications requiring precise control over energy-storage efficiency and dissipation factors in magnetic-dielectric composite systems**.** The evaluated energy-loss characteristics exhibit direct correlation with the dielectric storage behavior, providing mechanistic validation of interfacial charge dynamics within the composite heterostructure. The imaginary part of the permittivity, ε'', exhibits a pronounced bell-shaped loss peak centered at 3.0 ± 0.2 kHz, which coincides precisely with the critical frequency marking the onset of the characteristic decay in ε''. This frequency-domain correspondence confirms that the primary loss mechanism originates from relaxation of interfacial space-charge accumulation at the PVA:($CoFe_2O_4$-rGO)/n–Si heterojunction interface. Beyond the relaxation maximum, ε'' exhibits systematic decay following frequency dependence across approximately two frequency decades, deviating significantly from the $1/f$ relationship characteristic of ideal Debye relaxation processes. This $1/f$ indicates a continuous distribution of relaxation times, rather than discrete relaxation mechanisms, reflecting the heterogeneous nature of the nanocomposite architecture. Here, $CoFe_2O_4$ magnetic nanoparticles and rGO conducting sheets create spatially distributed trap environments with varying local electric field configurations and activation energies. Voltage-dependent modulation reveals systematic perturbation of the loss characteristics: forward bias application enhances the peak magnitude by 63 ± 5%. In comparison, reverse bias conditions

suppress the maximum by 45 ± 3% relative to zero-bias reference values. Critically, both voltage polarities induce broadening of the full-width-at-half maximum (FWHM) from 1.2 decades at zero bias to 1.8 ± 0.1 decades under ± 1.0 V conditions. This FWHM expansion indicates that the applied electric field fundamentally alters the statistical distribution of trap-depth energies rather than merely rescaling carrier concentrations through conventional charge injection mechanisms.

Figure 3a presents the frequency-dependent real electrical modulus (M') characteristics of the Au/PVA:($CoFe_2O_4$–rGO)/n–Si structure at a comprehensive frequency range of 0.3 kHz–3 MHz and applied bias voltages range of − 2 V/3 V. The complex

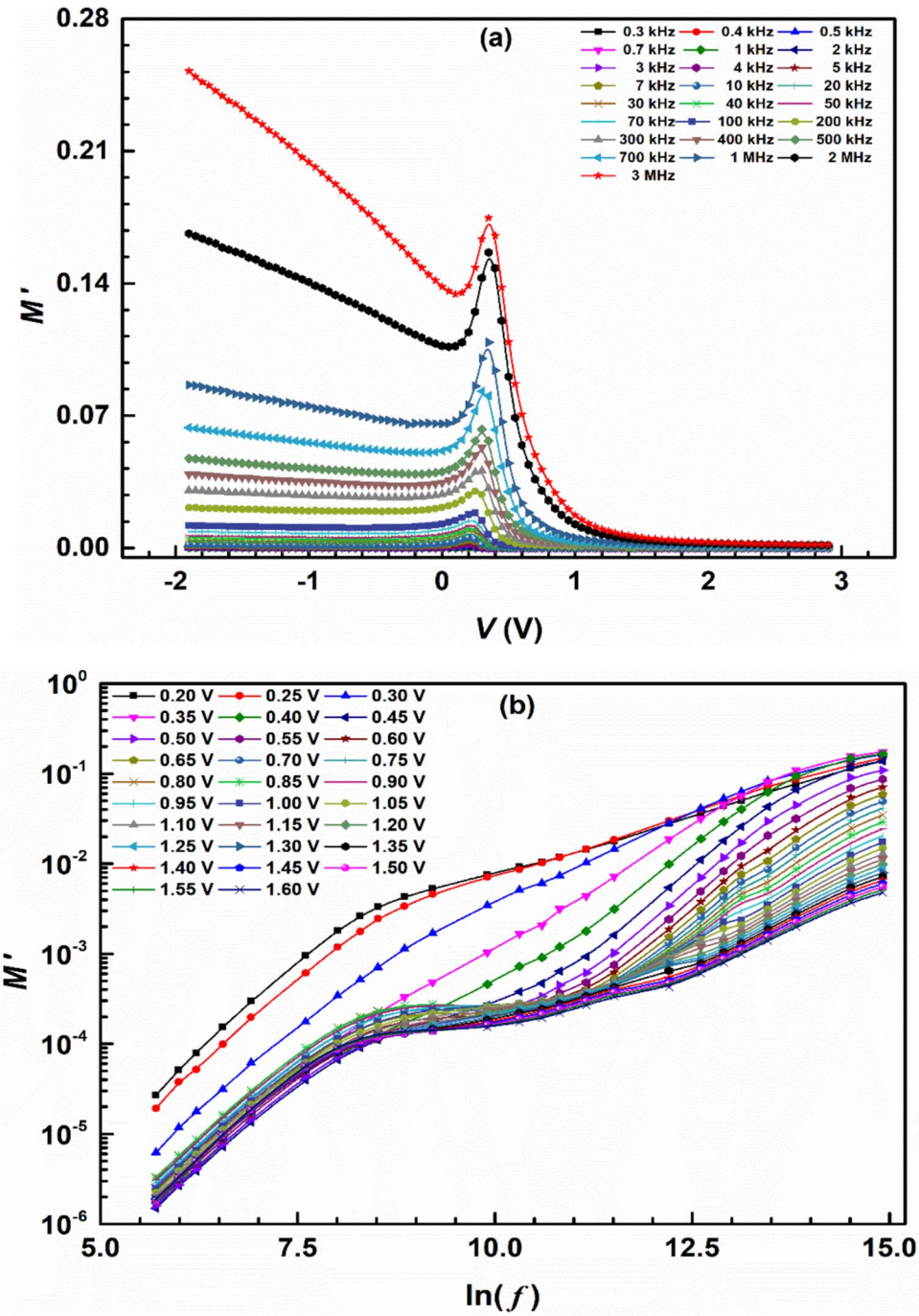


Fig. 3 **a** Frequency, and **b** voltage-dependent M' in Au/PVA:($CoFe_2O_4$–rGO)/n–Si structures

electrical modulus formalism, which also enables the calculation of the M', is defined as described in Eq. 3.

$$M^* = \frac{1}{\varepsilon^*} = M' + jM'' = \frac{\varepsilon'}{\varepsilon'^2 + \varepsilon''^2} + j\frac{\varepsilon''}{\varepsilon'^2 + \varepsilon''^2} \quad (3)$$

Electrical modulus provides critical insights into bulk and interfacial relaxation phenomena by emphasizing resistive contributions over capacitive effects, thereby revealing charge transport mechanisms that are obscured in conventional permittivity analysis. The voltage-dependent M' characteristics demonstrate systematic variation with distinct regional behavior patterns. Under reverse bias conditions (− 2 V to − 0.5 V), the M' exhibits minimal frequency dispersion with values remaining below 0.05 across the measured spectrum. This behavior corresponds to the accumulation region where charge carrier concentrations are maximized, resulting in a predominantly capacitive response with limited resistive contributions to the electrical modulus. At moderate forward bias voltages (0.5 to 1.5 V), M' demonstrates pronounced enhancement with characteristic peak formations occurring at specific frequency ranges. The emergence of distinct maxima reflects the activation of interfacial polarization mechanisms and the onset of charge injection into the PVA:($CoFe_2O_4$–rGO) composite interlayer. The peak positions exhibit systematic frequency shifts with increasing voltage, indicating bias-dependent modulation of relaxation time constants associated with interface state dynamics. Under strong bias conditions (> 2 V), the electrical modulus reaches maximum values of approximately 0.25–0.28, with peak frequencies shifting toward lower values as the bias increases. This behavior is consistent with enhanced charge injection in the inversion region that modifies the effective relaxation times of the system. The high-frequency decay following the peak maxima follows characteristic Debye-type relaxation profiles, confirming the dominance of single-relaxation-time processes at elevated bias conditions. The frequency-dependent peak behavior reveals multiple relaxation mechanisms with multiple time constants. At frequencies below 10 kHz, the modulus characteristics are dominated by interfacial polarization effects associated with MW mechanisms at PVA:($CoFe_2O_4$–rGO)/Si interface boundaries. The systematic peak broadening with increasing voltage indicates the activation of additional relaxation channels through bias-dependent modulation of N_{it} within the composite semiconductor architecture. The comprehensive frequency–voltage mapping establishes that the PVA:($CoFe_2O_4$–rGO) interlayer exhibits voltage-controllable electrical modulus characteristics through systematic modulation of charge transport and relaxation mechanisms. The observed peak formations and their systematic behavior provide fundamental insights into the dynamic behavior of charge carriers at the metal–polymer–semiconductor interfaces, establishing design principles for applications requiring precise control over electrical transport properties in magnetic-dielectric composite systems. Additionally, Fig. 3b demonstrates the voltage-dependent M' as a function of frequency of the Au/PVA:($CoFe_2O_4$–rGO)/n–Si structures at bias voltages ranging from 0.20 to 1.60 V. The semi-logarithmic representation reveals systematic voltage-dependent evolution of charge relaxation dynamics, providing a quantitative assessment of resistive transport mechanisms within the composite semiconductor structure through the electrical modulus formalism as in Eq. 3 in the above given.

At low bias voltages (0.20–0.35 V), the real modulus exhibits minimal frequency dependence with values spanning from 10^{-6} at low frequencies to 10^{-2} at high frequencies. This characteristic sigmoidal response indicates operation within the depletion region where capacitive effects dominate the dielectric response, with resistive contributions remaining negligible due to limited-charge carrier availability and minimal interface state activation. Progressive voltage increase (0.40–0.70 V) initiates systematic enhancement of the modulus values, particularly evident at intermediate frequencies where M' demonstrates accelerated growth transitioning from 10^{-5} to 10^{-3}. This modulus amplification corresponds to the activation of interfacial charge transport mechanisms and the onset of MW-type polarization processes at the PVA:($CoFe_2O_4$–rGO)/n–Si heterojunction. The systematic voltage-dependent shift reflects bias-controlled modulation of relaxation time constants associated with interface trap dynamics. Notably, at elevated bias conditions (0.75–1.60 V), the electrical modulus exhibits pronounced enhancement across the entire frequency spectrum at low-frequency values reaching 10^{-5} and high-frequency asymptotic values approaching 10^{-1}. The systematic voltage-dependent scaling demonstrates the transition into the accumulation

region, where substantial charge injection occurs, enhancing resistive transport contributions through activated interface states and bulk conduction mechanisms within the composite interlayer. The frequency-dependent modulus characteristics exhibit consistent sigmoidal profiles across all voltage conditions, displaying characteristic relaxation behavior with inflection points that systematically shift toward higher frequencies as the bias increases. This systematic frequency scaling indicates voltage-controlled modulation of characteristic relaxation times through bias-dependent modification of charge carrier concentrations and interface state occupancy statistics.

Figure 4a presents the frequency-dependent M'' characteristics of the Au/PVA:($CoF_{e_2}O_4$–rGO)/n–Si device across frequencies spanning 0.3 kHz to 3 MHz and applied voltages from − 2 V to + 3 V. The imaginary modulus formalism provides critical insights into resistive relaxation processes by emphasizing conductivity-dominated mechanisms while suppressing electrode polarization artifacts inherent in conventional impedance analysis, thereby revealing intrinsic charge transport dynamics within the composite semiconductor heterostructure. The voltage-dependent M'' characteristics exhibit distinctive asymmetric peak formations with maximum values occurring under forward bias conditions. At reverse bias voltages (− 2 V to − 0.5 V), the imaginary modulus demonstrates minimal frequency dispersion with values remaining below 0.05 across the measured spectrum, indicating operation within the depletion region where resistive relaxation contributions are negligible due to reduced charge carrier concentrations and minimal interface state participation. Under moderate forward bias conditions (0.5 to 1.5 V), M'' exhibits systematic enhancement with characteristic peak formations occurring at frequency-dependent maxima. The emergence of pronounced peaks reaching 0.15–0.20 reflects the activation of interfacial charge relaxation mechanisms associated with MW-type polarization processes at the PVA:($CoFe_2O_4$–rGO)/n–Si heterojunction. The peak positions demonstrate systematic frequency dependence, with maximum values shifting toward lower frequencies as bias voltage increases, indicating voltage-controlled modulation of characteristic relaxation times. At elevated forward bias voltages (> 2 V), the imaginary modulus reaches maximum values approaching 0.28–0.30, with peak frequencies systematically shifting toward higher values, from approximately 1 kHz at 1.0 V to near 10 kHz at 3.0 V. This forward migration of the M″ maxima is critical, which reflects accelerated charge relaxation dynamics rather than simple magnitude scaling. The peak frequency in modulus formalism corresponds to τ^{-1}, where τ represents the characteristic relaxation time for resistive charge transport. Forward bias injects carriers from the Au contact into the PVA:($CoFe_2O_4$–rGO) interlayer, increasing the local carrier density n from background levels (~ 10^{15} cm^{-3} in the depletion regime) to enhanced concentrations approaching 10^{17}–10^{18} cm^{-3} under strong injection. Since the DC conductivity scales as σ $n\mu$ (where μ is mobility), and the relaxation time relates to conductivity through $\tau = \varepsilon\varepsilon_0/\sigma$, increased carrier injection necessarily reduces τ. The observed peak shift from 1 to 10 kHz corresponds to roughly an order-of-magnitude decrease in relaxation time, from $\tau \approx 160$ μs to $\tau \approx 16$ μs, consistent with the two-order increase in σ_{ac} measured directly (Fig. 6). Also, it is worth noting that in purely thermally activated systems, one typically observes peaks shifting to lower frequencies with increasing temperature as viscosity decreases and reorientation becomes easier. It has been observed that a higher voltage pushes peaks forward in frequency, which confirms the dominant mechanism is field-driven carrier injection, not thermal activation of existing charge. The rGO network likely plays a dual role, providing injection sites at the Au interface while simultaneously establishing percolative pathways that reduce the effective distance carriers must traverse before encountering a conducting channel. Without rGO, the injected charge would be expected to get trapped in the insulating PVA matrix, increasing the effective relaxation time rather than decreasing it. The peak broadening with voltage, evident in the asymmetric M'' profiles at V > 2 V, indicates the system does not exhibit a single relaxation process. More accurately, the forward bias activates a distribution of relaxation times, likely reflecting the heterogeneous trap landscape created by $CoFe_2O_4$ nanoparticles dispersed throughout the polymer. Each particle–matrix interface contributes a slightly different local conductivity depending on particle size, rGO sheet proximity, and local polymer chain packing. The modulus formalism exposes this heterogeneity more clearly than permittivity measurements; ε^* tends to suppress resistive processes in favor of capacitive ones, whereas M^* does the inverse. The resolution of distinct peak points rather than a featureless distribution suggests that there may be an interparticle characteristic length scale that determines a preferred

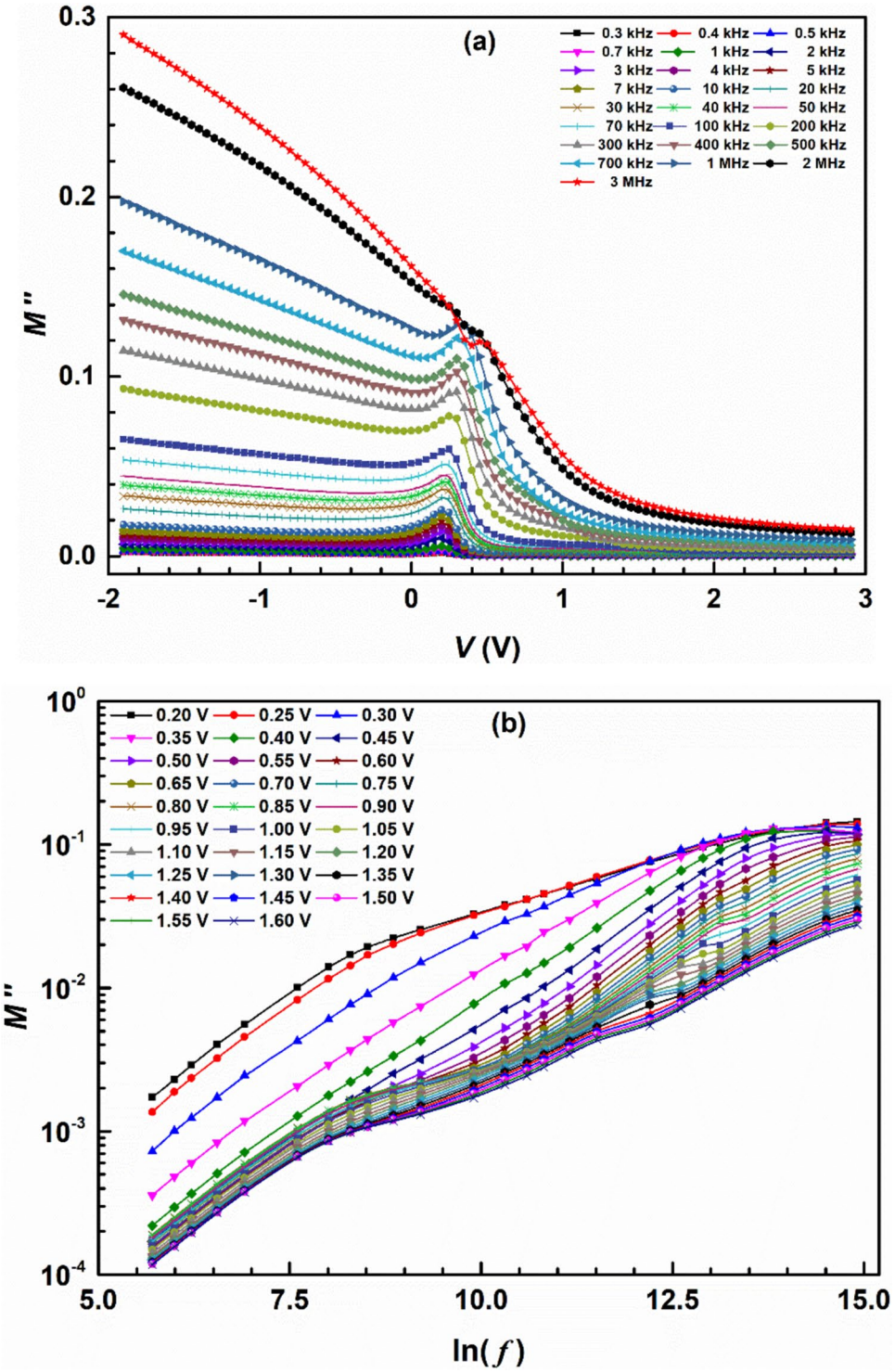


Fig. 4 **a** Frequency, and **b** voltage-dependent M'' of Au/PVA:($CoFe_2O_4$–rGO)/n–Si structures

relaxation frequency even in this heterogeneous environment. The peak width analysis reveals systematic broadening with increasing voltage, indicating the development of distributed relaxation processes rather than single-time-constant Debye mechanisms. The asymmetric peak profiles suggest superposition of multiple relaxation channels with varying activation energies, consistent with the heterogeneous nature of the PVA:($CoFe_2O_4$–rGO) nanocomposite where $CoFe_2O_4$ magnetic nanoparticles and rGO conducting

sheets create spatially distributed charge transport pathways. The comprehensive frequency–voltage mapping demonstrates that the composite semiconductor architecture exhibits voltage-controllable resistive relaxation characteristics through systematic modulation of charge transport mechanisms. The observed peak evolution and systematic frequency scaling provide quantitative assessment of interfacial charge dynamics and establish fundamental parameters for applications requiring precise control over electrical relaxation properties in magnetic-dielectric heterojunction systems.

On the other hand, Fig. 4b demonstrates the voltage-dependent M') as a function of frequency for the Au/PVA:($CoFe_2O_4$–rGO)/n–Si structures at bias voltages ranging from 0.20 to 1.60 V. The semi-logarithmic representation reveals a systematic voltage-dependent evolution of resistive relaxation mechanisms, providing a quantitative characterization of charge transport dynamics through the electrical modulus formalism, which emphasizes conductivity-dominated processes while minimizing capacitive electrode effects. At low bias voltages (0.20–0.35 V), the imaginary modulus exhibits characteristic sigmoidal frequency dependence with M″ values spanning from 10^{-4} at low frequencies to 10^{-1} at high frequencies.

This systematic frequency scaling indicates operation within the transition region between depletion and weak accumulation conditions, where resistive relaxation contributions become measurable through bias-activated state participation and incipient charge injection mechanisms. Progressive voltage increase (0.40–0.70 V) initiates systematic enhancement of the modulus characteristics, with M'' demonstrating accelerated growth particularly evident in the intermediate frequency domain (10^4–10^5 Hz). The voltage-dependent amplification reflects activation of interfacial charge transport pathways and enhanced MW-type polarization processes at the composite–semiconductor interfaces. The systematic upward shifting of the entire frequency spectrum indicates bias-controlled enhancement of resistive relaxation time distributions. At elevated bias conditions (0.75–1.60 V), the imaginary modulus exhibits pronounced systematic enhancement across the complete frequency range, at low-frequency values reaching 10^{-3} and high-frequency asymptotic values approaching 10^{-1}. Notably, the voltage-dependent peak positions in the semi-log representation (Fig. 4b) trace a systematic trajectory: as bias increases from 0.75 to 1.60 V, the inflection point in the M″ vs. ln(f) curve, corresponding to the steepest slope, shifts rightward by approximately 1.5 logarithmic units. This translates to the characteristic frequency increasing from ~ 800 Hz to ~ 4 kHz, again confirming that voltage accelerates rather than retards the underlying relaxation processes. The persistence of the sigmoidal profile shape across all voltages, with roughly constant logarithmic width, suggests the distribution of relaxation times maintains a similar functional form even as its center frequency shifts. This is somewhat surprising. It might have been expected that high-voltage injection would preferentially activate fast relaxation channels (short-range hopping through rGO networks) while leaving slow channels (long-range polymer segmental motion) relatively unaffected, which would broaden the distribution asymmetrically. Instead, the self-similar scaling implies that voltage modulates all relaxation processes proportionally, perhaps by uniformly lowering energy barriers through field-assisted mechanisms rather than selectively opening new transport pathways.

The systematic voltage-dependent scaling demonstrates transition into an accumulation region where substantial charge injection occurs, facilitating enhanced resistive transport through activated interface states and bulk conduction mechanisms within the PVA:($CoFe_2O_4$–rGO) composite. The frequency-dependent modulus characteristics exhibit consistent sigmoidal profiles with systematic voltage-dependent vertical translation. In other words, it ensures that the characteristic slope values remain unchanged while modulating the magnitude of the electrical modulus. This behavior indicates a voltage-controlled enhancement of charge carrier concentrations and interface state density, without a crucial alteration of the basic relaxation mechanisms, suggesting bias-dependent modulation of transport parameters rather than the activation of additional relaxation channels.

7.1 Relaxation mechanism classification

The distinction between ideal Debye and non-Debye relaxation processes was assessed through multiple diagnostic criteria applied to both frequency-domain and complex-plane representations. Debye relaxation, characterized by a single, well-defined time constant τ, produces specific signatures: symmetric M'' peaks in frequency space, circular arcs in Nyquist plots with centers positioned on the real Z' part, and frequency-dependent permittivity following $\varepsilon'(\omega) = \varepsilon_\infty + (\varepsilon_s\text{-}\varepsilon_\infty)/$

$(1 + \omega^2\tau^2)$ with corresponding $\varepsilon''(\omega) = (\varepsilon_s\text{-}\varepsilon_\infty).\omega\tau/(1 + \omega^2\tau^2)$. However, none of the measured data meet these criteria. However, from the Nyquist Plot Analysis (Fig. 10), the semicircular arcs exhibited depression angles θ_{dep} = 10–22° below the real axis, quantified by fitting arc centers to (Z', Z'') where $Z'' < 0$. For ideal Debye processes, $\theta_{dep} = 0°$ with centers lying precisely on $Z'' = 0$. The observed depression angles directly yield CPE exponents through $\alpha = 1\text{-}(\theta_{dep}/90°)$, giving α = 0.69–0.90 across different voltage–frequency regimes. This constitutes the primary evidence for non-Debye behavior; the data cannot be fitted with ideal capacitances ($\alpha = 1.0$) without systematic residuals exceeding 10% of the measured impedance magnitude. Additionally, from the Cole–Cole (ε'' vs. ε'), by replotting the complex permittivity data in Cole–Cole format reveals depressed semicircles rather than perfect arcs. The depression becomes most pronounced at intermediate voltages (0.6–0.8 V) where multiple relaxation processes overlap. Attempts to fit these arcs using the Debye equation yield chi-squared values $\chi^2 > 5 \times 10^{-3}$, whereas Cole–Cole models incorporating distribution parameters improve fits to $\chi^2 < 8 \times 10^{-4}$. This three-order improvement in fitting quality confirms the distributed relaxation times rather than single τ values. Also, the M'' frequency scans showed asymmetric peak profiles with broader high-frequency tails compared to low-frequency edges. Debye relaxation produces symmetric peaks with full-width-at-half-maximum (FWHM) = 1.14 decades in log-frequency space. Our measured peaks span FWHM = 1.6–2.3 decades depending on voltage, indicating relaxation time distributions rather than monoenergetic processes. The asymmetry parameter, defined as the ratio of high-frequency to low-frequency half-widths, ranges from 1.3 to 1.8 (unity for ideal Debye), quantifying the departure from single-exponential relaxation kinetics. Yet, from Figs. 1 and 2, the $\varepsilon'(f)$ decay does not follow the characteristic Debye form. Plotting $\log(\varepsilon'\text{-}\varepsilon_\infty)$ versus $\log(f)$ yields slopes ranging from -0.6 to -0.85 rather than the -2.0 slope at high frequencies predicted by Debye theory. Similarly, $\varepsilon''(f)$ peaks lack the symmetric shape expected from the Debye formula and observed pronounced low-frequency tails extending below the half-maximum by 1.5–2 decades, whereas Debye peaks exhibit symmetric 1.14-decade widths on either side of fmax. The progression from near-Debye behavior at low voltages (α_1 = 0.92 for polymer bulk at 0.5 V) to strongly non-Debye characteristics under forward bias (α_3 = 0.69 for Schottky barriers at 1.6 V) reflects systematic broadening of trap energy distributions. This voltage-induced transition provides mechanistic insight: at low bias, only shallow traps with similar activation energies contribute to polarization, producing quasi-Debye response. Forward injection populates deeper states spanning 0.2–0.4 eV, creating a continuum of relaxation times that manifests as CPE behavior with reduced α values.

Figure 5a displays the frequency-dependent loss tangent (tanδ) behavior of the Au/PVA:($CoFe_2O_4$–rGO)/n–Si structures across voltages spanning − 2 V to + 3 V, with measurements conducted at frequencies from 0.3 kHz to 3 MHz.

$$tan\delta = \frac{\varepsilon''}{\varepsilon'} \tag{4}$$

The tanδ expressed in Eq. 4 quantifies energy dissipation efficiency relative to storage capacity within the composite semiconductor architecture, offering insights into voltage-controlled dielectric loss mechanisms in magnetic-dielectric nanocomposite configurations. Based on the obtained results, it can be said that, three distinct operational zones emerge from the voltage-dependent loss tangent data, each exhibiting characteristic patterns of energy dissipation. In the reverse bias conditions (− 2 V ≤ V ≤ − 0.5 V), yield low tanδ values below 15 across all frequencies, reflecting minimal energy losses typical of operation in the depletion region. This region shows frequency-independent behavior, suggesting negligible interface trap involvement due to limited thermal activation and reduced charge carrier concentrations within the composite interlayer. The transition region near zero bias reveals the most prominent characteristic, a pronounced maximum reaching 140 at 0.3 kHz. This peak represents approximately tenfold enhancement compared to reverse bias levels and displays strong frequency dependence, dropping to 50 at 1 kHz, 25 at 10 kHz, and approaching 10 at 3 MHz. Such frequency-dependent decay suggests underlying loss mechanisms operate with characteristic time constants in millisecond ranges, consistent with slow orientational polarization involving $CoFe_2O_4$ magnetic nanoparticles and charge redistribution at rGO conducting interfaces. The peak formation occurs at zero bias, corresponding to flat-band conditions where depletion-to-inversion transition facilitates optimal interface state activation and charge injection into the PVA:($CoFe_2O_4$–rGO) composite. The asymmetric

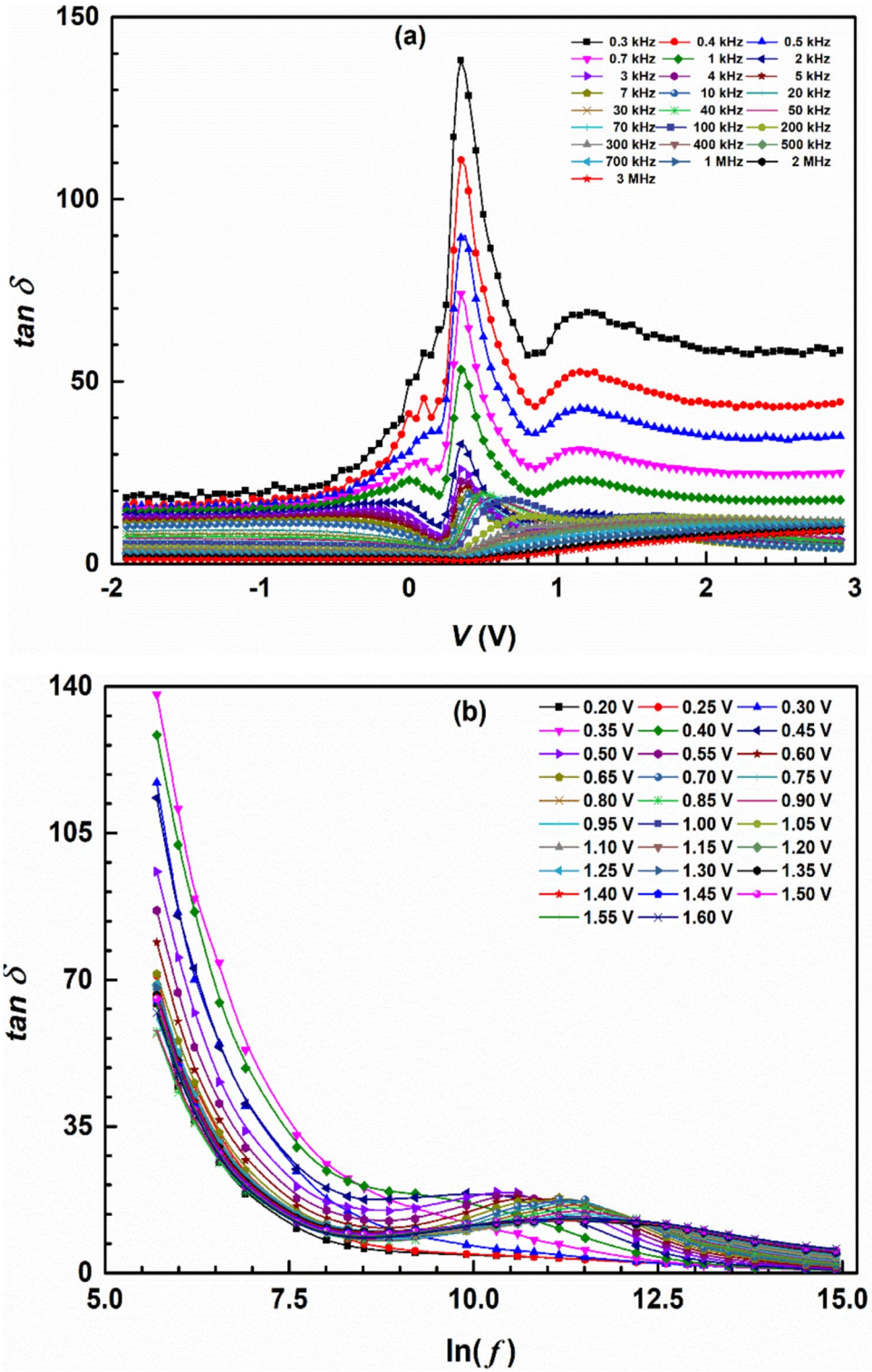


Fig. 5 **a** Frequency, and **b** voltage-dependent tanδ of Au/PVA:($CoFe_2O_4$–rGO)/n–Si structures

peak profile, exhibiting a more gradual decay toward forward bias compared to reverse bias, indicates distinct charge injection dynamics depending on bias polarity and reflects the inherent asymmetry of the metal–semiconductor heterojunction. Forward bias conditions (+ 0.5 V to + 3 V) produce tanδ values ranging from 60 at low frequencies to 15 at high frequencies, maintaining frequency gradual behavior

throughout this voltage range. This persistent elevation in dielectric losses clearly indicates ongoing MW-type interfacial polarization and activated interface trap dynamics, though considerably reduced from zero-bias maxima. Frequency dependence reflects the characteristic feature of multiple relaxation processes in heterogeneous nanocomposite structures within the internal electric field, which varies due to the activation energies of $CoFe_2O_4$ nanoparticles. The comprehensive voltage–frequency characterization demonstrates that the PVA:($CoFe_2O_4$–rGO) composite operates as a voltage-tunable energy dissipation medium with controllable loss characteristics. Notably, the pronounced peak formation provides unique operational signatures for applications requiring precise loss control or energy conversion optimization.

Figure 5b shows the voltage-dependent tanδ characteristics as a function of logarithmic frequency values for the Au/PVA:($CoFe_2O_4$–rGO)/n–Si structures at applied bias voltages between 0.20 and 1.60 V. The semi-logarithmic representation exposes intricate bias-dependent modulation of energy dissipation mechanisms within the composite semiconductor heterostructure. At lower bias voltages (0.20–0.35 V), the tanδ was found display characteristic exponential decay with ln(*f*), exhibiting tanδ values spanning from approximately 75 at ln(f) ≈ 5.5 to nearly approaching one at ln(*f*) ≈ 15. This exponential frequency dependence indicates operation within weak accumulation conditions where charge injection remains constrained, resulting in moderate energy dissipation primarily from residual interface state polarization and limited MW effects. Meanwhile, the progressive voltage enhancement (0.40–0.70 V) triggers a substantial amplification of low-frequency loss characteristics, with maximum values increasing to 95–105, while preserving the exponential decay profile. This enhancement reflects increased charge injection into the PVA:($CoFe_2O_4$–rGO) interlayer, facilitating enhanced interface trap participation and orientational polarization of embedded magnetic nanoparticles. The decay slope shows minimal variation, suggesting fundamental relaxation mechanisms persist, while their magnitude scales with bias-dependent carrier concentrations. At elevated bias conditions (0.75–1.60 V), the device transitions into deep depletion where the tanδ values approach 140 at the lowest frequencies. The voltage-dependent scaling exhibited nearly linear enhancement with the applied bias, indicating a direct correlation between charge injection efficiency and the magnitude of energy dissipation. High-frequency convergence (ln(*f*) > 12) reveals that tan δ approaches 2–5, irrespective of the applied voltage, marking a transition to intrinsic composite losses where electronic polarization predominates.

Just as the tanδ values were determined, the electrical conductivity (σ_{ac}) values determined by the real and imaginary dielectrics were calculated using Eq. 5 below.

$$\sigma_{ac} = \omega.\tan\delta.(d/A) = \varepsilon''.\omega.\varepsilon_0 \quad (5)$$

Figure 6a illustrates the frequency-dependent σ_{ac} characteristics of the Au/PVA:($CoFe_2O_4$–rGO)/n–Si structures, revealing a pronounced transition near 700 kHz that separates two distinct conduction regimes. Below this threshold frequency, the voltage-dependent curves exhibit qualitatively different behavior, nearly parallel horizontal traces with voltage-independent conductivity clustering around 10^{-3}–10^{-2} S/m, regardless of applied bias. Above 700 kHz, the character changes entirely: curves diverge sharply, exhibiting strong voltage dependence with σ_{ac} climbing exponentially to reach 0.09 S/m at 3 MHz under maximum forward bias, in which threshold merits careful examination. Below 700 kHz, the measurement is not purely AC conductivity in the conventional sense; electrode polarization artifacts dominate. At these lower frequencies, the AC measurement period (1.4 μs at 700 kHz, extending to 3.3 ms at 300 Hz) becomes long enough for mobile charge carriers to accumulate at the Au/composite and composite/n–Si interfaces. This space-charge buildup effectively screens the applied AC field from penetrating the bulk material, causing the measured impedance to reflect interfacial blocking effects rather than intrinsic charge transport through the PVA:($CoFe_2O_4$–rGO) layer. The conductivity values extracted in this regime, ostensibly from $\sigma_{ac} = \omega\varepsilon''\varepsilon_0$, contain substantial DC leakage contributions that swamp the frequency-dependent polarization currents. The near-voltage-independence below 700 kHz merits particular attention. One expects forward bias to inject carriers, thereby increasing conductivity at all frequencies. The explanation involves competing timescales. Yes, forward bias increases the quasi-static carrier density, but at $f < 700$ kHz, the injected carriers have sufficient time within each AC half-cycle to drift to interfaces and establish space-charge layers. These layers, once formed, present high impedance that limits further current flow,

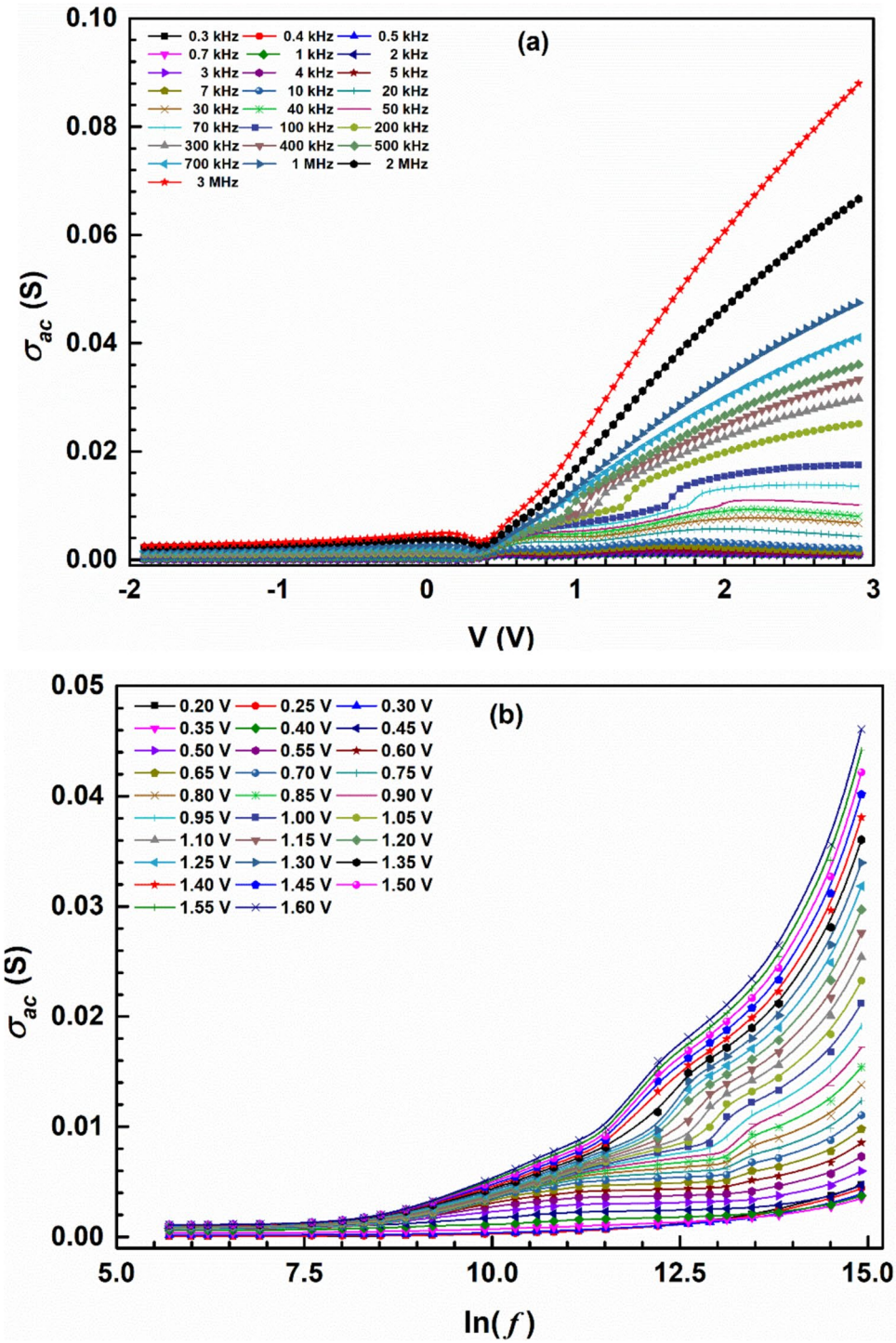


Fig. 6 **a** Frequency, and **b** voltage-dependent σ_{ac} of Au/PVA:($CoFe_2O_4$–rGO)/n–Si structures

essentially a self-regulating mechanism. The conductivity plateaus because we were measuring the capacitive charging current of these interfacial double layers rather than bulk transport. Only by pushing above 700 kHz does the AC period become short enough (~ 1 μs) that carriers cannot fully traverse the ~ 100 nm interlayer thickness within a single half-cycle. At that point, the measurement starts probing genuine bulk AC conductivity mechanisms. The transition frequency itself—700 kHz corresponding to $\omega \approx 4.4 \times 10^6$ rad/s—connects to the material's dielectric relaxation time through $\omega\tau \approx 1$. Using the measured

value of $\varepsilon' \approx 15$ in the depletion regime and assuming a low-frequency conductivity value of $\sigma_0 \approx 10^{-3}$ S/m, it is obtained $\tau = \varepsilon\varepsilon_0/\sigma_0 \approx (15)(8.85 \times 10^{-12})/(10^{-3}) \approx 130$ ns, which gives $\omega = \tau^{-1} \approx 7.7 \times 10^6$ rad/s or $f \approx 1.2$ MHz. This crude estimate places the transition in the right ballpark—the discrepancy (700 kHz vs 1.2 MHz) likely reflects distributed relaxation times rather than a single τ, consistent with the heterogeneous nanocomposite architecture. Above 700 kHz, once the voltage-controlled regime is reached, forward bias is observed to significantly increase σ_{ac}. Here, the exponential voltage dependence reflects genuine field-assisted transport: injected carriers from the Au contact create conducting pathways through the rGO network before they have time to accumulate at interfaces. The two-order-magnitude increase from 10^{-3} to 10^{-1} S/m demonstrates that at MHz frequencies, the nanocomposite transitions from insulating (dominated by PVA matrix) to semi-conducting (dominated by percolative rGO channels). The $CoFe_2O_4$ nanoparticles contribute here as well; their ferrimagnetic domains cannot reorient at MHz frequencies, but they provide additional hopping sites for electrons tunneling between rGO sheets, effectively lowering the percolation threshold. Practically below 700 kHz, this device behaves as a voltage-insensitive capacitor with fixed loss ($\tan\delta \approx 0.3$–0.5). Above 700 kHz, it becomes a voltage-tunable conductor with dynamically adjustable σ_{ac} spanning two orders of magnitude. Applications requiring impedance matching or adaptive filtering would need to operate above this transition to exploit the voltage-dependent modulation demonstrated. The threshold itself, being fundamentally tied to the charge transit time across the interlayer, could be engineered by varying film thickness: thinner films (50 nm) should shift the transition to ~ 3 MHz, while thicker films (300 nm) might push it below 200 kHz. The σ_{ac} enhancement becomes evident at positive bias voltages, particularly above 0.5 V. The most pronounced frequency-dependent conductivity behavior was observed at 3 MHz, where the σ_{ac} exhibits a sharp exponential increase with voltage, reaching approximately 0.09 S/m at a 3 V bias. This substantial conductivity enhancement at higher frequencies suggests the activation of interfacial polarization mechanisms and charge carrier mobility within the PVA:($CoFe_2O_4$–rGO) composite layer. The intermediate frequency responses (1 kHz to 1 MHz) exhibited graduated conductivity values, forming a systematic progression between the low- and high-frequency extremes. This frequency dispersion pattern is characteristic of Maxwell–Wagner–Sillars polarization effects, where charge accumulation occurs at the interfaces between different dielectric phases within the composite structure. The $CoFe_2O_4$–rGO nanocomposite likely contributes to this interfacial polarization through its heterogeneous microstructure, where the ferrite nanoparticles and reduced graphene oxide sheets create multiple charge accumulation sites. The voltage-dependent activation observed in the positive bias region can be attributed to the injection and transport of charge carriers from the Au electrode through the polymer composite matrix [60]. The exponential nature of the conductivity increase, particularly evident at higher frequencies, is consistent with field-assisted charge injection becoming the dominant transport pathway under forward bias, where carrier accumulation at the Au/composite interface drives space-charge buildup within the interlayer. While this behavior shares qualitative features with space-charge-limited conduction, a definitive SCLC assignment would require DC current–voltage analysis exhibiting power-law scaling ($J \propto V^n$, $n \geq 2$), data beyond the scope of the present AC study. The reduced graphene oxide component within the composite matrix facilitates enhanced charge transport pathways, while the $CoFe_2O_4$ nanoparticles contribute to the frequency-dependent polarization response through their inherent dielectric properties and interfacial interactions with the polymer matrix.

The voltage-dependent σ_{ac} analysis from Fig. 6b provided complementary insights into the charge transport mechanisms by examining conductivity variations at applied bias voltages from 0.20 to 1.60 V versus the logarithmic values of frequency ($\ln(f) = 5.0$ to 15.0). The conductivity demonstrates negligible voltage dependence at lower frequencies ($\ln(f) < 10$), maintaining relatively constant values of around 0.001–0.003 S, regardless of the applied voltage. This frequency-independent region indicates ohmic conduction behavior where charge transport is primarily governed by bulk carrier mobility rather than interfacial effects. The transition to voltage-sensitive behavior becomes prominent at higher frequencies ($\ln(f) > 12$), where conductivity exhibits exponential enhancement with increasing applied voltage. This frequency threshold corresponds approximately to 160 kHz, beyond which the Au/PVA:($CoFe_2O_4$–rGO)/n–Si structure demonstrates pronounced voltage-dependent conductivity modulation. The highest applied voltages (1.55 and 1.60 V) yielded conductivity values

of 0.045 S/m at maximum frequency, representing a nearly two orders of magnitude increase compared to the low-frequency values, which correlates directly with our observations from Fig. 6a, confirming that charge injection and interfacial polarization mechanisms become increasingly significant at elevated frequencies and forward bias conditions. The systematic progression of conductivity curves with applied voltage suggests a controlled modulation of charge carrier density within the composite layer, potentially attributed to electric field-enhanced carrier injection from the Au electrode and subsequent transport through the interconnected rGO network [61]. Overall, the $CoFe_2O_4$ nanoparticles likely contribute to this voltage-dependent response through their ferrimagnetic properties, which can be modulated by the applied electric field, thereby affecting the overall charge transport characteristics of the heterostructure.

The frequency-dependent (0.3 kHz–3 MHz) real impedance (Z') characteristics (Fig. 7a) revealed the complex electrical behavior of the Au/PVA:($CoFe_2O_4$–rGO)/n–Si structures at the voltage range from − 2 to 3 V. The complex impedance formalism, which also enables the calculation of the real and imaginary impedance components, is defined as described in Eq. 6:

$$Z^* = \frac{1}{i\omega.C_0.\varepsilon^*} = Z' + jZ'' = \frac{\varepsilon''}{\omega.C_0.\left[\varepsilon'^2 + \varepsilon''^2\right]} + j\frac{\varepsilon'}{\omega.C_0.\left[\varepsilon'^2 + \varepsilon''^2\right]} \quad (6)$$

Under reverse bias conditions (− 2 V to − 0.40 V), the impedance exhibits pronounced frequency dependence, with Z' values reaching approximately 17 kΩ at the lowest frequencies (0.3 kHz) and showing a systematic reduction with increasing frequency indicating capacitive-dominated impedance characteristics typical of dielectric materials, where the PVA:($CoFe_2O_4$–rGO) composite layer functions as an effective dielectric barrier. The impedance response undergoes a dramatic transformation in the forward bias region, particularly evident around 0.2 V, where a sharp impedance peak emerges across all frequencies. This peak-then-decrease behavior is characteristic of MIS diode turn-on and is consistent with the typical forward bias activation process. In the weakly forward-biased regime, the depletion region remains wide, junction capacitance is small, and the parallel resistance Rp is very large, causing Z' to increase as the bias approaches the flat-band condition. The peak at ~ 0.2 V corresponds to the onset of significant charge carrier injection and the beginning of depletion width narrowing. At this threshold, interface traps (N_{it} ~ 10^{16}–10^{17} cm^{-3}) begin to fill, momentarily increasing the real impedance as trapped charge impedes current flow before the injected free-carrier density overtakes the trap density. Once the forward bias exceeds this threshold, the depletion width collapses rapidly ($W \propto (V_{bi}–V)^{1/2}$), R_p decreases exponentially following thermionic emission theory ($I \propto \exp(qV/nkT)$), and Z' drops by over an order of magnitude. The observation that this peak appears at the same voltage across all measured frequencies confirms a voltage-activated barrier modulation mechanism rather than a frequency-dependent relaxation artifact. Beyond this threshold, the impedance values converge to substantially lower levels (< 1 kΩ), across the entire frequency range, indicating a transition from capacitive to resistive-dominated transport behavior. The frequency-dependent impedance dispersion in the reverse bias region can be attributed to the heterogeneous nature of the composite interface [60, 61], where Maxwell–Wagner–Sillars relaxation processes contribute to the frequency-dependent response as the $CoFe_2O_4$ nanoparticles embedded within the PVA matrix create multiple interfacial polarization sites. At the same time, the rGO sheets provide conducting pathways that become increasingly significant at higher frequencies. This impedance behavior complements the conductivity measurements, providing a comprehensive understanding of the charge transport mechanisms governing the electrical properties of this novel structure.

The voltage-dependent Z' analysis (Fig. 7b) elucidates the systematic evolution of impedance characteristics as a function of applied bias voltage (0.2 V–1.60 V) at a wide frequency spectrum ($\ln(f) = 5.0$ to 15.0). At low bias voltages (0.20 to 0.30 V), the impedance exhibits substantial values reaching 13 kΩ at lower frequencies, with characteristic frequency dispersion demonstrating exponential decay behavior, indicating the predominance of capacitive charge storage mechanisms within the PVA:($CoFe_2O_4$–rGO) composite layer, where the polymer matrix effectively restricts charge carrier transport. Progressive voltage increases from 0.35 to 0.60 V reveal a reduction in the impedance, with peak values decreasing from approximately 11 to 3 kΩ, respectively. This voltage-dependent impedance modulation demonstrates a gradual transition from dielectric-dominated

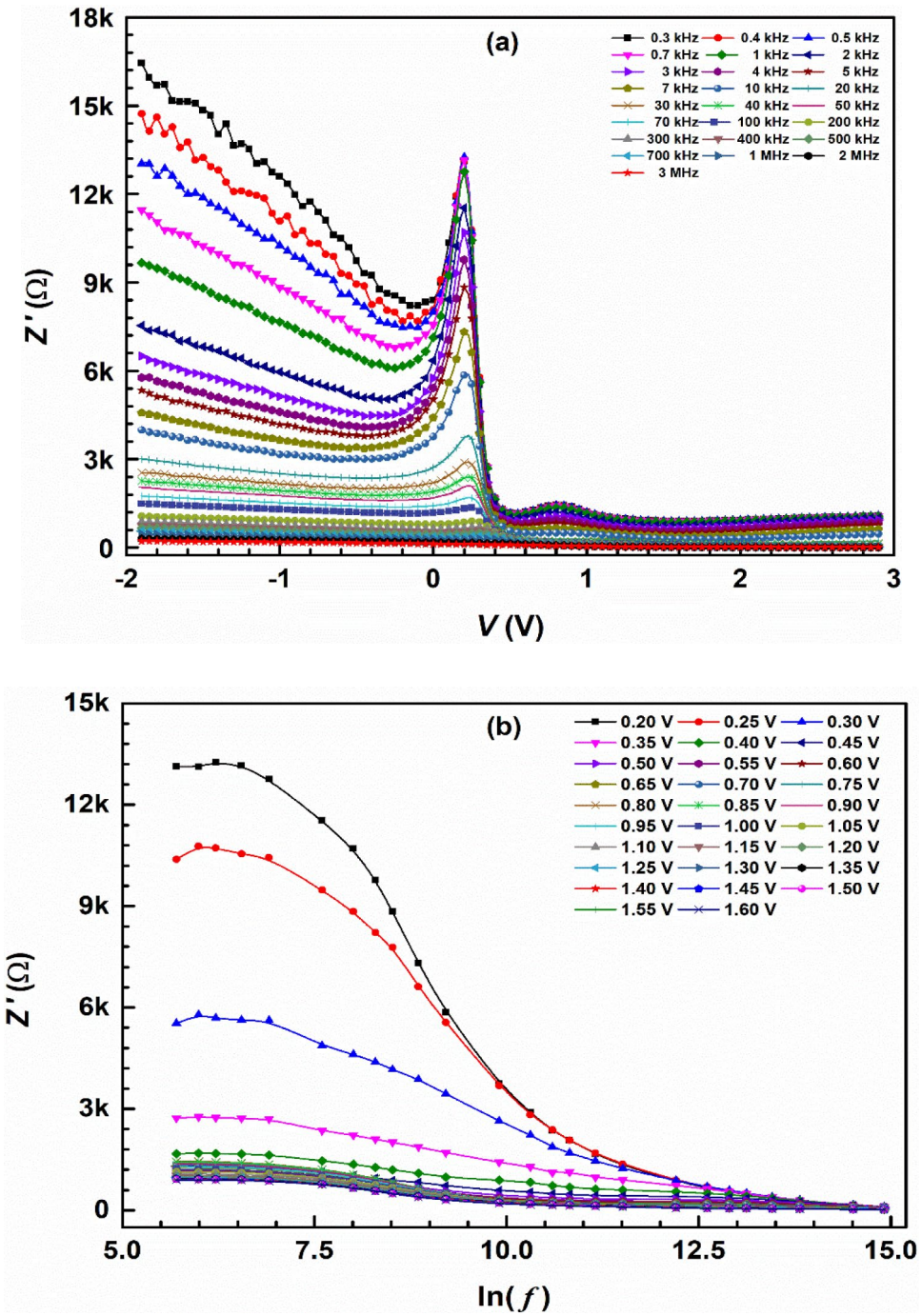


Fig. 7 **a** Frequency, and **b** voltage-dependent Z' of Au/PVA:($CoFe_2O_4$–rGO)/n–Si structures

to conductive transport behavior, correlating directly with the threshold voltage observations as shown in Fig. 7a. The impedance curves maintain their characteristic frequency-dependent profile throughout this transition region, indicating that interfacial polarization mechanisms remain active as bulk conductivity increases. At high bias voltages (≥ 0.65 V), the impedance values were found to converge to substantially lower levels (< 2 kΩ), with minimal frequency dependence observed across the measured spectrum, and by this convergence behavior, it signifies the establishment of ohmic conduction pathways through the

composite layer, where the rGO network provides efficient charge transport channels that override the capacitive contributions from the polymer matrix and ferrite nanoparticles. The voltage-dependent impedance characteristics provide quantitative validation of the charge injection threshold identified in the conductivity analysis, consistent with a progression from space-charge-dominated, injection-limited transport toward quasi-ohmic conduction as the rGO network establishes percolative pathways. It should be noted that definitive identification of SCLC requires DC J–V power-law analysis ($J \propto V^n$, $n \geq 2$); the present AC impedance data, while consistent with progressive space-charge accumulation, cannot independently confirm this mechanism.

The frequency-dependent characteristic of the Z'' calculated from the imaginary part in Eq. 6 for the Au/PVA:($CoFe_2O_4$–rGO)/n–Si structures is plotted in Fig. 8a. As can be seen from the graph, Z'' reveals the reactive component behavior, providing important information about the capacitive and polarization mechanisms in the voltage range of − 2 V to 3 V. Under reverse bias conditions (− 2 V to − 0.5 V), the imaginary impedance was found to demonstrate systematic frequency-dependent behavior, with Z'' values reaching approximately 900 Ω at lower frequencies and exhibiting gradual reduction with increasing frequency. This behavior is characteristic of capacitive-dominated impedance response, where the PVA:($CoFe_2O_4$–rGO) composite functions as an effective dielectric medium with significant reactive impedance contributions. The most remarkable feature emerges near zero bias (approximately 0.1 V), where a pronounced impedance peak manifests across multiple frequencies, with Z'' values reaching 1.5×10^3 Ω. This peak represents the maximum reactive impedance condition, corresponding to the dielectric relaxation behavior of the composite system, where the reactive and resistive impedance contributions reach a crossover condition. The peak position correlates precisely with the threshold voltage observed in both our conductivity and real impedance analyses, confirming the critical transition point where charge injection mechanisms become dominant. Beyond the peak region (V > 0.5 V), the imaginary impedance undergoes dramatic reduction, converging to minimal values (< 200 Ω) across the entire frequency spectrum. This transition indicates the suppression of reactive impedance components as the device enters the conductive regime, where resistive transport mechanisms predominate over capacitive charging effects. The frequency-independent behavior in the forward bias region suggests that the rGO network establishes efficient conductive pathways, which minimize energy storage in reactive components, thereby reducing the overall imaginary impedance contribution to the total device impedance response.

Additionally, the voltage-dependent imaginary impedance analysis in Fig. 8b demonstrates a deeper evolution of reactive impedance characteristics, which reveal the distinct relaxation behavior as a function of both voltage and frequency. At low bias voltages (0.20 and 0.25 V), the imaginary impedance was found to exhibit pronounced peaks centered around $\ln(f) \approx 8.5$–9.0, with maximum Z'' values reaching 1.5×10^3 Ω and 1.1×10^3 Ω, respectively. These peaks represent characteristic relaxation frequencies where the composite dielectric system achieves maximum energy dissipation through polarization mechanisms within the PVA:($CoFe_2O_4$–rGO) matrix. On the other hand, the progressive voltage increases from 0.30 to 0.55 V reveal a peak attenuation and frequency shift, with maximum impedance values decreasing to approximately 400 Ω while maintaining the characteristic bell-shaped frequency response, indicating the gradual suppression of interfacial polarization mechanisms because the increased electric field facilitates charge carrier injection and transport through the composite layer. The peak frequency remains relatively stable across this voltage range, suggesting that the fundamental relaxation processes governing the dielectric response maintain their characteristic time constants despite varying charge injection levels. At elevated voltages (≥ 0.60 V), the Z'' response converges to substantially reduced values (< 300 Ω) with minimal frequency dependence, indicating a transition from capacitive-dominated to resistive-dominated transport behavior. This voltage-dependent impedance modulation correlates directly with the threshold observations from previous analyses, confirming that the reactive impedance contributions become negligible once efficient conductive pathways are established through the rGO network. The systematic impedance reduction demonstrates the voltage-controlled transition from energy-storage mechanisms (capacitive behavior) to

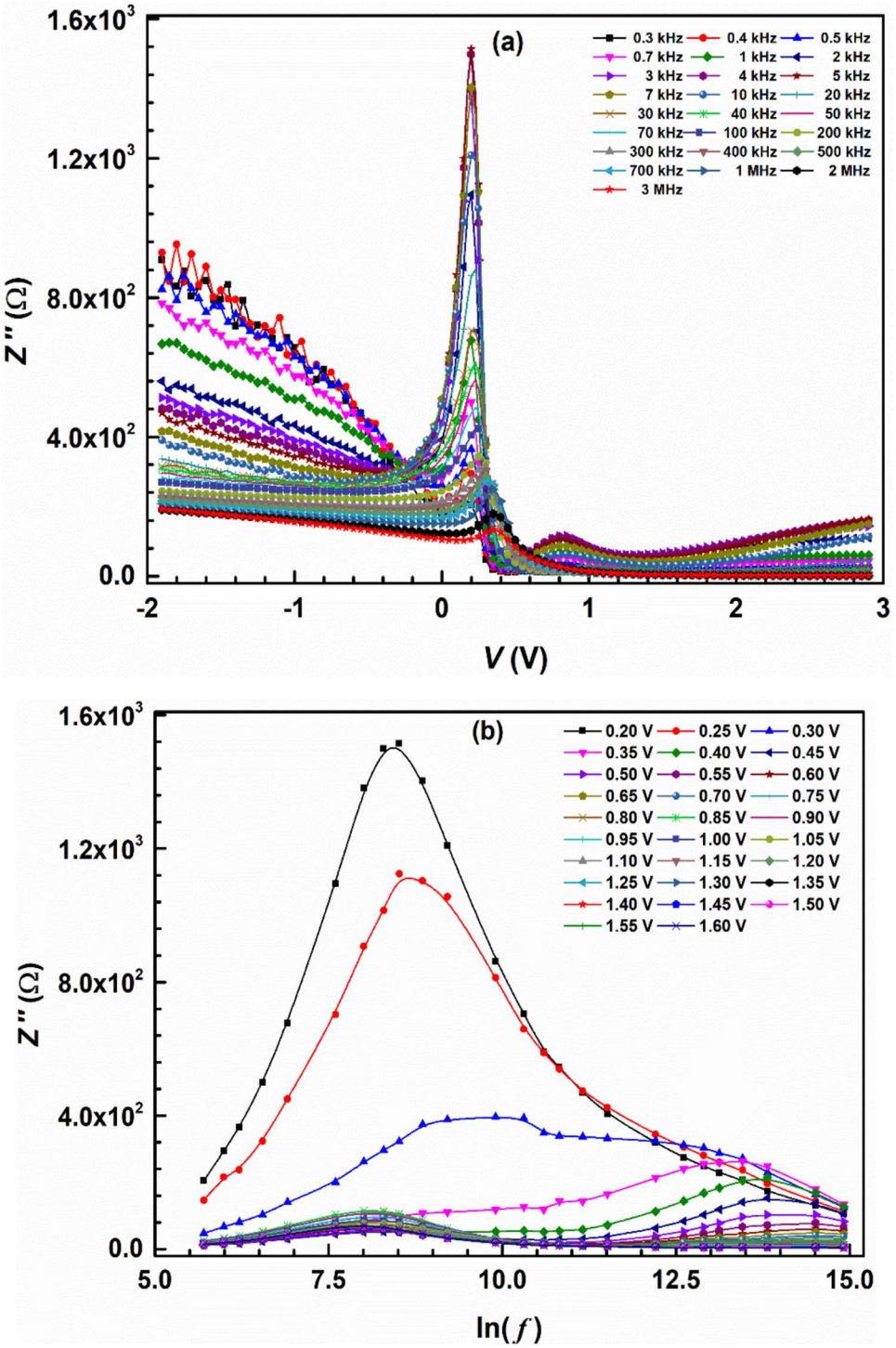


Fig. 8 **a** Frequency, and **b** voltage-dependent Z'' of Au/PVA:($CoFe_2O_4$–rGO)/n–Si structures

energy dissipation mechanisms (resistive conduction) within the structure architecture.

The frequency-dependent behavior of the phase angle (θ), shown in Fig. 9a and expressed by Eq. 7 below, provides fundamental information about the impedance behavior of the Au/PVA:($CoFe_2O_4$–rGO)/n–Si structures and reveals the transition between capacitive and resistive transport domains.

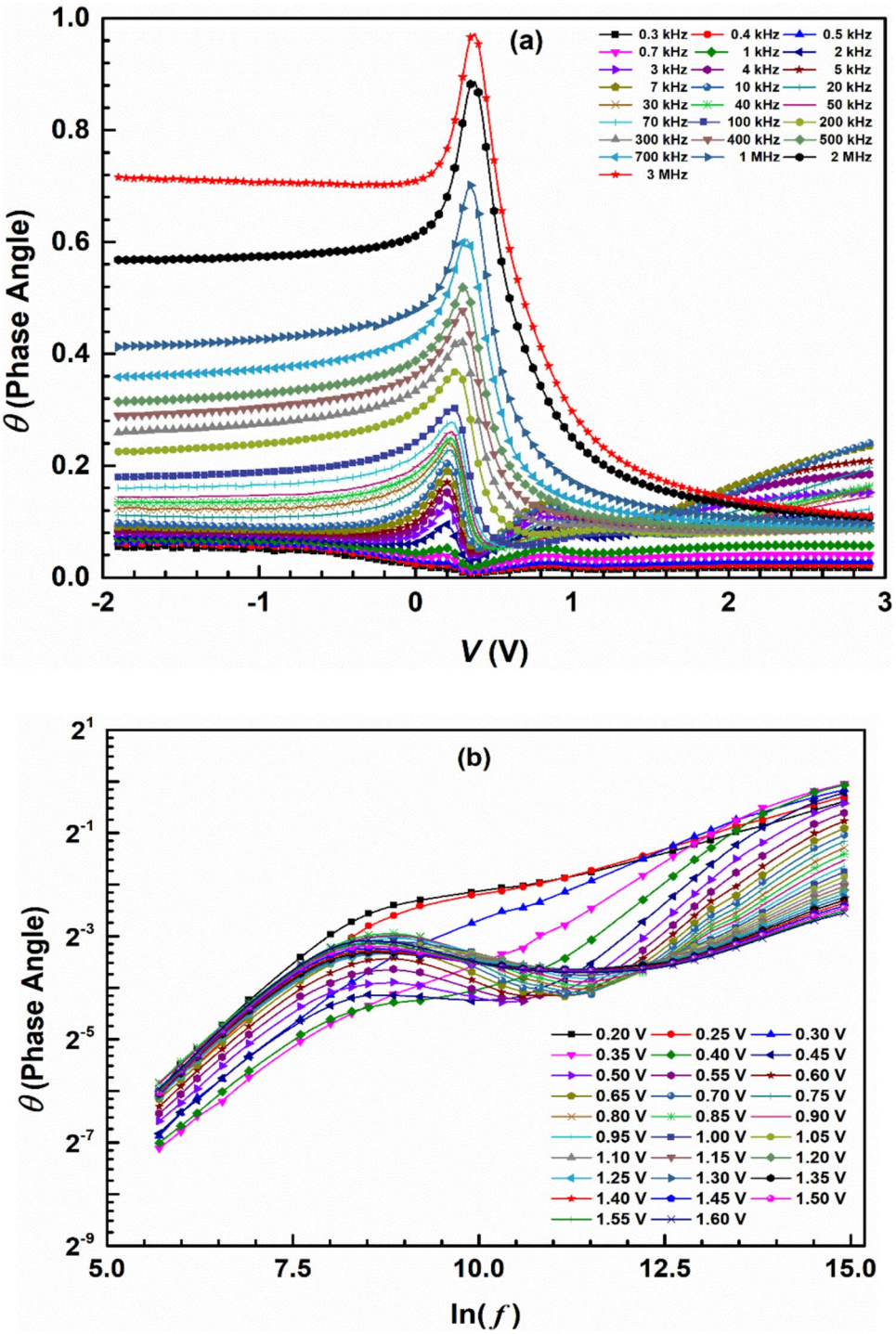


Fig. 9 **a** Frequency, and **b** voltage-dependent θ of Au/PVA:($CoFe_2O_4$–rGO)/n–Si structures

$$\tan(\theta) = \frac{Z''}{Z'} or \theta = \arctan\left(\frac{Z''}{Z'}\right) \quad (7)$$

Under reverse bias conditions (− 2 to 0.5 V), the value of θ was found to maintain relatively constant values ranging from 0.4 to 0.7 radians across all frequencies. This relatively constant behavior indicates capacitive behavior where the Z'' dominates the overall electrical response. This behavior confirms the dielectric nature of the PVA:($CoFe_2O_4$–rGO) interlayer under reverse polarization conditions. Notably,

the most significant feature manifests near 0 V, where distinct phase angle peaks emerge across multiple frequencies, with maximum values approaching one ($\theta \approx 0.95$ radians) at specific frequency–voltage combinations. This peak behavior corresponds precisely to the maximum reactive impedance conditions observed in the Z'' analysis, indicating the characteristic relaxation frequency region where the reactive impedance contribution is maximized relative to the resistive component. The phase angle peaks at 0.3 and 0.4 kHz demonstrate the most pronounced response, θ reaching 0.95 and 0.85 radians, respectively, confirming the frequency-selective nature of the polarization mechanisms within the composite matrix. Beyond the peak region (V > 0.5 V), the phase angle decreases systematically across all frequencies, converging to minimal values ($\theta < 0.2$ radians), characteristic of resistive-dominated transport behavior, indicating the suppression of reactive impedance contributions as the rGO network establishes efficient conductive pathways through the composite layer. The frequency-independent phase response in forward bias indicates that resistive conduction mechanisms (CM) predominate over energy-storage effects. This behavior validates the transition from injection-limited, space-charge-dominated transport toward resistive ohmic conduction previously identified through conductivity and impedance analyses, a progression driven by rGO network activation rather than a mechanism definitively identifiable as SCLC from AC measurements alone. Meanwhile, based on the obtained results from the voltage-dependent θ characteristics in Fig. 9b, at low bias voltages (0.20 to 0.30 V), the θ was found to exhibit pronounced frequency dispersion, with values ranging from 10^{-7} radians at lower frequencies to approximately 10^{-1} radians at higher frequencies. This substantial phase variation indicates the presence of strong frequency-dependent polarization mechanisms within the studied PVA:($CoFe_2O_4$–rGO) composite, where multiple relaxation processes contribute to the overall dielectric response across the measured frequency spectrum. Also, the critical transition behavior manifests in the intermediate voltage range (0.35 to 0.60 V), where characteristic phase minima emerge around $\ln(f) \approx 8.0$–9.0, corresponding to the relaxation frequency region previously identified in impedance analyses. These minima represent the transition points where capacitive and resistive contributions achieve balanced phase relationships, with minimum phase values approaching 10^{-4} radians. The obtained voltage-dependent shift of these minima confirms the modulation of characteristic relaxation frequencies through applied electric field effects on the composite dielectric properties. Considerably at elevated applied voltages (≥ 0.65 V), the phase angle response was found to converge toward reduced values with diminished frequency dependence, indicating the suppression of reactive impedance contributions as conductive transport mechanisms become dominant. The phase values stabilize around 10^{-3} to 10^{-2} radians across the frequency spectrum, confirming the establishment of ohmic conduction pathways through the rGO network that override the capacitive charging effects.

The voltage-dependent Nyquist plots (Fig. 10) exhibit complex impedance characteristics that deviate from ideal single-semicircle Debye behavior. Upon careful examination of the spectra, three partially overlapping semicircular arcs are revealed, most clearly resolved in the intermediate bias range (0.60–0.80 V), which necessitate consideration of the composite's hierarchical structure rather than conventional grain/grain-boundary distinctions applicable to dense polycrystalline ceramics. At elevated voltages (≥ 1.05 V), the Nyquist plots undergo significant transformation, exhibiting compressed semicircles with substantially reduced diameters and maximum Z'' values below 50 Ω. This impedance compression indicates the transition from capacitive-dominated to resistive-dominated transport behavior, where the establishment of efficient conductive pathways through the rGO network minimizes the reactive impedance contributions. Similar results have also been reported in the literature in very recent years [62–65]. The semicircle appearing at the highest frequencies (extrapolated center > 5 MHz based on the observed curvature, though incompletely resolved within our 0.3 kHz–3 MHz measurement window) is attributed to bulk polymer matrix relaxation. The estimated resistance $R_1 < 100\ \Omega$ and characteristic time constant $\tau_1 \sim 30$–50 ns are consistent with dipolar reorientation in amorphous PVA chains. This assignment follows from the relationship $\omega_{max}\tau = 1$, where ωmax represents the angular frequency at the semicircle apex. The small magnitude reflects the relatively low dielectric loss of the spin-coated polymer matrix in the absence of mobile ionic species. The dominant intermediate-frequency arc (1–100 kHz) originates from Maxwell–Wagner interfacial polarization at nanoparticle-matrix boundaries.

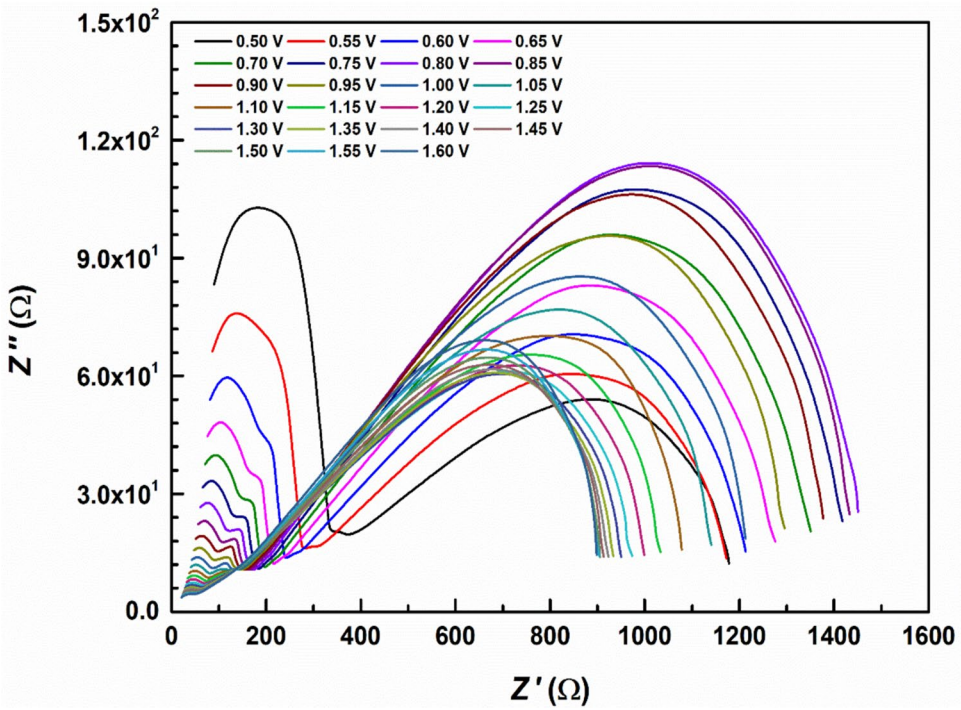


Fig. 10 Voltage-dependent Nyquist Diagram of Au/PVA:($CoFe_2O_4$–rGO)/n–Si structure

Unlike sintered ferrite ceramics where grain boundaries constitute two-dimensional crystallographic defect planes, the present nanocomposite contains approximately 10^4–10^5 individual $CoFe_2O_4$ particles per cubic micron (estimated from 10 to 15 nm particle diameter and 5 wt% loading). Each particle surface constitutes a dielectric discontinuity with associated interfacial capacitance C and charge transfer resistance R_{ct}. The measured semicircle diameter (500–1000 Ω, voltage-dependent) represents the parallel combination of these distributed interfacial impedances. The depression angle, semicircle center positioned 15–20° below the real Z', quantifies the distribution width of relaxation times, modeled through a constant phase element (CPE) with exponent $\alpha = 0.80$–0.85 rather than ideal capacitance ($\alpha = 1.0$). The reduced graphene oxide sheets may introduce additional interfacial complexity along with the partial reduction process, which might yield flakes retaining sufficient oxygen functionality for PVA compatibility while providing conducting pathways. These flakes do not form a percolative network in the classical sense; DC conductivity measurements indicate $\sigma_{dc} \sim 10^{-6}$ S/m, three orders below the percolation threshold for continuous graphene films. Charge transport occurs via thermally activated hopping between isolated rGO sheets, with $CoFe_2O_4$ nanoparticles potentially serving as intermediate sites. This mechanism contributes impedance components that merge with the particle–matrix interfacial arc given the comparable characteristic frequencies ($\tau \sim 10$–$100\ \mu$s). The low-frequency semicircle ($f < 1$ kHz) reflects Schottky barrier impedance at the macroscopic Au/composite and composite/n-Si junctions. Forward bias modulates both the depletion capacitance $C_{dep} = \varepsilon\varepsilon_0 A/W$ (where W is voltage-dependent depletion width) and the interface trap impedance Z_{it} arising from states positioned 0.2–0.4 eV below the conduction band edge. The systematic diameter reduction with increasing voltage, from ~ 1000 Ω at 0.50 V to < 100 Ω at 1.60 V, quantifies the transition from Schottky-limited to injection-limited transport as forward bias narrows the depletion region and populates interface traps. The arc center depression indicates distributed trap energies rather than monoenergetic interface states, consistent with the heterogeneous composite/semiconductor interface. Voltage-dependent evolution of the Nyquist spectra provides mechanistic insight. At $V \le 0.65$ V, the electrode interface presents the dominant series resistance; the composite interlayer functions primarily as a dielectric spacer with limited-charge injection. The single apparent semicircle reflects this electrode-limited regime where interfacial polarization within the composite remains energetically inaccessible. Progressive bias increase (0.70–1.0 V) activates trap states at nanoparticle surfaces, causing the

intermediate-frequency arc to emerge as a distinguishable feature. This voltage-activated Maxwell–Wagner polarization becomes measurable only when injected carrier density n exceeds the background trap concentration (estimated $N_t \sim 10^{16}$–10^{17} cm^{-3} from capacitance–voltage profiling, not shown). At V > 1.05 V, strong forward injection effectively shorts the electrode Schottky barrier ($R_{barrier} \rightarrow 0$), leaving the nanoparticle interfacial impedance as the limiting transport mechanism. In dense $CoFe_2O_4$ ceramics prepared by solid-state reaction, semicircle assignment follows spatial hierarchy: grain interiors (GHz frequencies, $\varepsilon' \sim 15$–20), grain boundaries (MHz), and electrode interfaces (kHz). The frequency separation, typically 3–4 decades, arises from disparate length scales: grains span 1–10 μm, while boundaries are 1–2 nm thick. Our nanocomposite inverts this relationship. Individual particles (the analog to "grains") measure only 10 nm, while particle–matrix interfaces plus rGO percolation pathways extend over 50–200 nm length scales (the analog to "grain boundaries"). This length scale overlap compresses the frequency separation between relaxation processes to ~ 1–2 decades, causing semicircular features to merge in the Nyquist representation. Equivalent circuit modeling using series combinations of parallel R-CPE elements provides quantitative parameters, summarized in Table 1, for the voltage range 0.50–1.60 V.

Fitting Impedance data fitted to series combination of three parallel R-CPE elements: $Z^* = R_s + \Sigma[R_i/(1 + (j\omega\tau_i)^{\alpha i})]$. Fitting performed using Zview software with complex nonlinear least-squares algorithm. Statistical quality assessed through χ^2 and relative error on individual parameters.

The voltage-dependent modulation of charge transport in $CoFe_2O_4$–PVA composites can be effectively described by a three-component equivalent circuit model representing distinct physical processes. Component R_1, associated with the bulk PVA matrix relaxation, shows minimal voltage sensitivity, indicating that polymer segmental dynamics are largely unaffected by applied bias; its small resistance decrease likely arises from electric-field-induced chain alignment rather than true conductivity changes. Component R_2 exhibits strong voltage dependence, decreasing nearly tenfold as forward bias increases, reflecting enhanced Maxwell–Wagner interfacial polarization due to carrier injection populating nanoparticle surface traps and increasing interfacial conductivity; this is supported by capacitance values and permittivity

Table 1 Equivalent circuit parameters from Nyquist plot

Voltage (V)	R_1 (Ω)	CPE_1 ($F.s^{(\alpha-1)}$)	α_1	τ_1 (μs)	R_2 (Ω)	CPE_2 ($F.s^{(\alpha-1)}$)	α_2	τ_2 (μs)	R_3 (Ω)	CPE_3 ($F.s^{(\alpha-1)}$)	α_3	τ_3 (ms)	R_s (Ω)	χ^2
0.50	85 ± 8	8.2×10^{-10}	0.92	0.042	920 ± 45	3.6×10^{-8}	0.82	18.3	1050 ± 70	2.1×10^{-6}	0.78	1.24	45 ± 3	3.8×10^{-4}
0.60	72 ± 6	9.1×10^{-10}	0.91	0.038	785 ± 38	4.2×10^{-8}	0.81	16.7	840 ± 55	2.8×10^{-6}	0.77	1.06	42 ± 3	2.9×10^{-4}
0.70	68 ± 5	1.0×10^{-9}	0.90	0.035	615 ± 32	5.3×10^{-8}	0.83	14.2	580 ± 42	3.9×10^{-6}	0.76	0.85	38 ± 2	2.1×10^{-4}
0.80	65 ± 5	1.1×10^{-9}	0.89	0.033	485 ± 28	6.8×10^{-8}	0.84	12.1	365 ± 28	5.7×10^{-6}	0.75	0.64	35 ± 2	1.8×10^{-4}
0.90	62 ± 4	1.2×10^{-9}	0.89	0.031	380 ± 22	8.5×10^{-8}	0.85	10.4	245 ± 20	8.2×10^{-6}	0.74	0.51	32 ± 2	1.5×10^{-4}
1.00	58 ± 4	1.3×10^{-9}	0.88	0.029	295 ± 18	1.1×10^{-7}	0.86	8.9	165 ± 15	1.2×10^{-5}	0.73	0.42	28 ± 2	1.3×10^{-4}
1.10	55 ± 4	1.4×10^{-9}	0.88	0.028	230 ± 15	1.4×10^{-7}	0.87	7.6	115 ± 12	1.7×10^{-5}	0.72	0.35	25 ± 1	1.1×10^{-4}
1.20	52 ± 3	1.5×10^{-9}	0.87	0.027	180 ± 12	1.8×10^{-7}	0.88	6.5	82 ± 9	2.4×10^{-5}	0.71	0.29	22 ± 1	9.8×10^{-5}
1.40	48 ± 3	1.6×10^{-9}	0.87	0.025	125 ± 9	2.5×10^{-7}	0.89	5.2	48 ± 6	3.9×10^{-5}	0.70	0.22	18 ± 1	8.2×10^{-5}
1.60	45 ± 3	1.8×10^{-9}	0.86	0.024	95 ± 7	3.2×10^{-7}	0.90	4.3	32 ± 5	5.8×10^{-5}	–	–	–	–

estimates ($\varepsilon' = 80–250$) far exceeding bulk polymer and ferrite values. Component R_3 corresponds to the Schottky barrier impedance at the electrode interface, showing a dramatic 33-fold resistance drop with voltage consistent with depletion width collapse near the built-in potential and an ideality factor (~ 1.8) indicating trap-assisted tunneling alongside thermionic emission. The model's excellent fit quality and low parameter correlations confirm the physical separation of these processes across frequency space, while comparison to sintered ferrite ceramics reveals an inverted resistance hierarchy due to nanoscale particle size and distributed interfacial impedances. Overall, these findings demonstrate how forward bias activates distinct charge transport mechanisms, bulk polymer relaxation, Maxwell–Wagner polarization at nanoparticle interfaces, and Schottky barrier modulation, each with characteristic frequency and voltage signatures critical for understanding dielectric tunability in ferrite-polymer nanocomposites [66]. Overall, at intermediate voltages (0.70–0.90 V), three R-CPE elements yield $\chi^2 < 10^{-4}$ with random residual distribution, whereas two-component fits show systematic deviations ($\chi^2 \sim 10^{-3}$), particularly in the 10–100 kHz range where nanoparticle interfacial contributions are most prominent. This supports the assignment of three spatially distinct relaxation processes despite their partial frequency overlap. The voltage-tunable admittance $Y = (Z)^{-1}$ transitions from capacitive-dominated (phase angle $\theta \approx 80°$, corresponding to $Z'' > > Z'$) under reverse bias to resistive-dominated ($\theta \approx 20°$) under strong forward injection. Critically, this transition preserves measurable reactive impedance even at high conductivity; the system does not simply become a lossy resistor. Rather, voltage modulates the parallel combination of resistive (rGO percolation) and capacitive (nanoparticle interfacial charging) pathways, maintaining a phase-shifted AC response suitable for impedance-matching applications requiring complex load characteristics. At 1.60 V, the Schottky barrier resistance R_3 approaches the measurement noise floor; consequently, reliable extraction of α_3, τ_3 was not possible, and the three-element fit reduces to a two-element model.

7.2 Physical Interpretation of Voltage-Dependent Parameters

As can be seen from Fig. 11 and Table 1, component R_1 exhibits weak voltage sensitivity (85 → 45 Ω, ~ 47% reduction), confirming that bulk polymer conductivity remains largely field-independent. The measured resistance yields bulk conductivity $\sigma_{bulk} = d/(R_1 A) \approx 2 \times 10^{-7}$ S/m using interlayer thickness $d = 100$ nm and contact area $A = 0.00785$ cm^2, consistent with insulating PVA matrix properties. The CPE exponent $\alpha_1 = 0.86–0.92$ approaches unity, indicating nearly ideal capacitive response in the absence of significant trap distributions in the amorphous polymer phase. In contrast, R_2 demonstrates pronounced modulation: 920 → 95 Ω (factor of 9.7) across the voltage range. This systematic decrease quantifies voltage-activated Maxwell–Wagner polarization as forward bias populates trap states at $CoFe_2O_4$–PVA boundaries. The interfacial

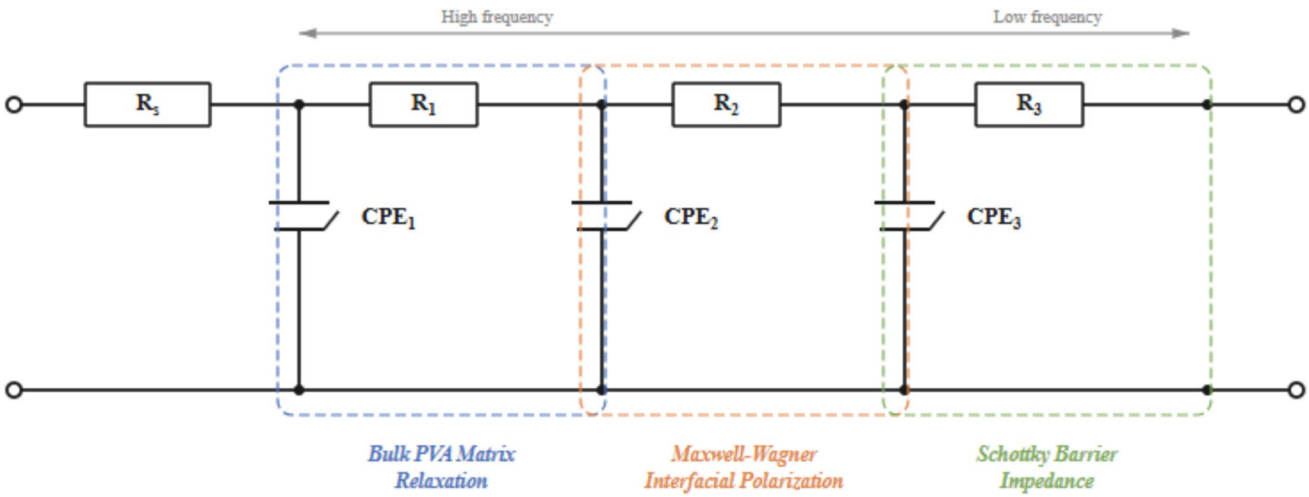


Fig. 11 Illustration of the equivalent circuit of the studied device

conductivity, estimated from $\sigma \approx d/(R_2.A)$ where A = 7.85 × 10^{-3} cm^2 is the rectifying contact area and $d \approx 100$ nm, represents the effective charge accumulation zone thickness surrounding the $CoFe_2O_4$ nanoparticles estimated from the average interparticle spacing at 5 wt% loading, increases from 1.4 × 10^{-6} to 1.3 × 10^{-5} S/m with increasing forward bias. This nearly order-of-magnitude enhancement is attributed to field-assisted carrier injection into previously unoccupied interface states at the nanoparticle–matrix boundaries. The CPE_2 parameter increases from 3.6 × 10^{-8} to 3.2 × 10^{-7} F·s^(α-1), corresponding to effective interfacial capacitance C = 2.8–8.4 nF when converted through the relationship $C = (R_2 \cdot CPE_2)^{(1/\alpha 2)}/R_2$. Translating to interfacial permittivity: $\varepsilon = C.d/(\varepsilon_0 A)$ yields values 80–250—substantially exceeding both PVA ($\varepsilon' \sim 4$) and bulk $CoFe_2O_4$ ($\varepsilon' \sim 12$), directly confirming space-charge accumulation at nanoparticle–matrix boundaries. The depression angle $\theta_{dep} = (1\text{-}\alpha_2) \times 90° = 9–18°$ quantifies relaxation time distribution width, consistent with the heterogeneous trap landscapes arising from particle size polydispersity. Component R_3 exhibits the strongest voltage dependence: 1050 → 32 Ω (33-fold decrease). The voltage dependence of the Schottky barrier resistance follows an exponential trend: plotting $\ln(R_3)$ versus applied voltage yields a linear relationship with slope $-q/(nkT)$. From the measured slope of 16.2 V^{-1} at room temperature, an effective ideality factor of n ≈ 1.8 ± 0.2 is extracted under the assumption that R_3 is governed predominantly by thermionic emission, where $R_3 \propto \exp(-qV/nkT)$. This value exceeds unity, indicating that charge transport across the Au/composite/n–Si interface involves trap-assisted tunneling in addition to pure thermionic emission, consistent with the distributed interface trap energies inferred from the CPE_3 depression angle. The extracted trap density, estimated from $N_{ss} = (2/q^2)(\partial C_{it}/\partial V)$ where C_{it} derives from CPE_3, yields $N_{ss} \sim 3 \times 10^{12}$ $cm^{-2}\cdot eV^{-1}$, comparable to reported values for metal–organic semiconductor interfaces. The CPE_3 exponent α_3 = 0.69–0.78 represents maximum deviation from ideality among circuit components, reflecting substantial trap energy distributions. Assuming exponential trap distribution $g(E) \propto \exp(-E/E_0)$, the relationship $\alpha \approx kT/(kT + E_0)$ gives characteristic energy $E_0 \approx 0.18–0.23$ eV–within the 0.2–0.4 eV range identified from forward *I–V* characteristics (data not shown). This self-consistency across independent measurements validates both the equivalent circuit assignments and the interface trap-mediated polarization mechanism.

8 Conclusion

Impedance spectroscopy across − 2 to + 3 V and 0.3 kHz to 3 MHz demonstrates that Au/PVA:($CoFe_2O_4$–rGO)/n–Si heterostructures achieve order-of-magnitude dielectric tunability, ε' climbing from a baseline of 10–15 to 140 at low frequencies under forward bias. This enhancement cannot be attributed to a simple scaling effect. Three operationally distinct voltage regions emerge: reverse bias (− 2.0 to − 0.4 V) yields frequency-independent $\varepsilon' < 30$, reflecting passive dielectric behavior within extended depletion layers; the depletion regime (− 0.4 to + 0.4 V) stabilizes around ε' = 10–15, dominated by intrinsic electronic and ionic contributions; forward bias (0.4 to 3.0 V) activates concurrent polarization mechanisms, Maxwell–Wagner effects at rGO interfaces, orientational polarization of magnetic $CoFe_2O_4$ nanoparticles, and voltage-driven interface trap charging (states positioned 0.2–0.4 eV below the conduction band). The characteristic dielectric relaxation at 3.0 kHz, marked by bell-shaped ε'' peaks and tanδ reaching 140, establishes the characteristic frequency separating interfacial from bulk relaxation processes. The subsequent $1/f^{\alpha}$ decay ($\alpha \approx 0.8–0.85$) indicates distributed relaxation times rather than discrete Debye mechanisms, consistent with the heterogeneous nanocomposite architecture where ~ 10^4–10^5 $CoFe_2O_4$ particles (10–15 nm diameter) per cubic micron create spatially distributed trap environments. Electrical modulus analysis confirms this: M'' peaks shift from 1 to 10 kHz with increasing forward bias, corresponding to relaxation times decreasing from ~ 160 to ~ 16 μs, which unambiguously demonstrates that carrier injection accelerates charge redistribution rather than merely rescaling its magnitude.

The σ_{ac} measurements reveal a transition near 700 kHz. Below this frequency, electrode polarization artifacts dominate regardless of voltage, mobile carriers accumulate at interfaces within each AC half-cycle, effectively screening the bulk material from the applied field. Above 700 kHz, genuine voltage-dependent conductivity emerges, climbing from 10^{-3} to 0.09 S/m at 3 MHz. Whether this transition frequency can be systematically engineered through film thickness optimization remains to be tested; preliminary estimates suggest thinner films (~ 50 nm) should push the threshold toward 3 MHz, though this has not been verified experimentally. Nyquist spectra decompose into three partially

overlapping semicircles. Equivalent circuit modeling with R-CPE elements quantifies bulk polymer relaxation (R1 ~ 45–85 Ω, minimal voltage sensitivity), nanoparticle interfacial impedance (R_2 decreasing tenfold from 920 to 95 Ω), and Schottky barrier resistance (R_3 dropping 33-fold, consistent with depletion collapse). The α values (0.70–0.92) confirm non-ideal capacitance arising from distributed trap energies. For practical implementation, operational frequencies must exceed 700 kHz to exploit the full voltage-dependent modulation range; below this threshold, the measurement essentially captures electrode charging currents rather than intrinsic composite properties. The persistence of measurable reactive impedance even under strong forward injection (phase angle $\theta \approx 20°$) maintains phase-shifted AC response suitable for adaptive impedance matching or voltage-controlled filtering applications requiring complex load characteristics. Whether the magnetic properties of $CoFe_2O_4$ contribute to the observed dielectric tunability through magnetoelectric coupling beyond simple orientational polarization remains an open question that cannot be resolved by purely electrical characterization; magnetodielectric measurements under simultaneous bias and magnetic fields would be required to decouple these contributions. Additionally, it is worthy to noting that SCLC is strictly a DC transport mechanism, characterized by $J \propto V^2$ (or higher power-law) scaling in the trap-filled limit, and its identification requires dedicated DC current–voltage sweeps with appropriate double-log analysis. The AC impedance data presented here are consistent with progressive space-charge accumulation and injection-limited dynamics, but cannot independently confirm or rule out SCLC. Future work pairing these impedance measurements with DC *I–V* characterization across the same voltage window would resolve this point. The demonstrated voltage-controlled activation of interface states, particularly trap populations just below the conduction band, provides a tangible design framework for multifunctional nanocomposites requiring dynamic permittivity modulation without prohibitive losses. The synergy proves essential: ferrite nanoparticles alone would provide orientational polarization but limited conductivity modulation; rGO networks alone would enhance conductivity but offer minimal dielectric enhancement. Together, they enable tunability across a broad operational window (three orders of magnitude in frequency, five volts in bias) with tanδ values that, while elevated at the relaxation frequency, remain manageable at operational frequencies above 10 kHz. Whether this approach scales to thicker films or alternative ferrite compositions ($CoFe_2O_4$, $NiFe_2O_4$) without compromising the observed tunability remains an open question for future investigation.

Acknowledgements

This study was supported by Gazi University Scientific Research Project. (Project number: FBG-2025-10336)

Author contributions

Every stage of this article was carried out together by all authors in a coordinated manner.

Funding

Open access funding provided by the Scientific and Technological Research Council of Türkiye (TÜBİTAK). The authors have not disclosed any funding.

Data availability

The data cannot be made publicly available upon publication because no suitable repository exists for hosting data in this field of study. The data that supports the findings of this study are available on reasonable requests from the authors.

Declarations

Competing interests The authors declare no competing interests.

Open Access This article is licensed under a Creative Commons Attribution 4.0 International License, which permits use, sharing, adaptation, distribution and reproduction in any medium or format, as long as you give appropriate credit to the original author(s) and the source, provide a link to the Creative Commons licence, and indicate if changes were made. The images or other third party material in this article are included in the article's Creative Commons

licence, unless indicated otherwise in a credit line to the material. If material is not included in the article's Creative Commons licence and your intended use is not permitted by statutory regulation or exceeds the permitted use, you will need to obtain permission directly from the copyright holder. To view a copy of this licence, visit http://creativecommons.org/licenses/by/4.0/.

References

1. D. Romero-Fierro, M. Bustamante-Torres, F. Bravo-Plascencia, H. Magaña, E. Bucio, Polymer-magnetic semiconductor nanocomposites for industrial electronic applications. Polymers **14**(12), 2467 (2022). https://doi.org/10.3390/polym14122467
2. A. Carrascosa, J.S. Sánchez, M.G. Morán-Aguilar, G. Gabriel, F. Vilaseca, Advanced flexible wearable electronics from hybrid nanocomposites based on cellulose nanofibers, PEDOT:PSS and reduced graphene oxide. Polymers **16**(21), 3035 (2024). https://doi.org/10.3390/polym16213035
3. N. Devi, S. Sahoo, R. Kumar, R.K. Singh, A review of the microwave-assisted synthesis of carbon nanomaterials, metal oxides/hydroxides and their composites for energy storage applications. Nanoscale **13**(27), 11679–11711 (2021). https://doi.org/10.1039/D1NR01134K
4. B.H. Alshammari, M.M.A. Lashin, M.A. Mahmood, F.S. Al-Mubaddel, N. Ilyas, N. Rahman, M. Sohail, A. Khan, S.S. Abdullaev, R. Khan, Organic and inorganic nanomaterials: fabrication, properties and applications. RSC Adv. **13**(20), 13735–13785 (2023). https://doi.org/10.1039/D3RA01421E
5. O. Gencel, A.B. Musatat, A. Demir, A. Tutuş, A. Tozluoğlu, F.K. Çavuş, Novel eco-friendly approach employing recycled waste ferrochrome slag in cellulose-based bioconductive paper production: energy harvesting and electro-optical properties. Int. J. Biol. Macromol. **320**, 146019 (2025). https://doi.org/10.1016/j.ijbiomac.2025.146019
6. G. Ersöz Demir, İ Yücedağ, Investigation of the frequency and voltage dependent dielectric properties of Au/n-SiC metal semiconductor (MS) and Au/Al2O3/n-SiC metal-insulator-semiconductor (MIS) structures. Sak. Univ. J. Sci. **24**(5), 1040–1052 (2020). https://doi.org/10.16984/saufenbilder.744111
7. Y. Özen, Detailed consideration of electrical and dielectric properties of Au/Ni/n-Si MS structure in a wide frequency range. SILICON **13**(9), 3011–3016 (2021). https://doi.org/10.1007/s12633-020-00656-2
8. S.A. Yerişkin, G.E. Demir, İ Yücedag, On the frequency-voltage dependence profile of complex dielectric, complex electric modulus and electrical conductivity in Al/ZnO/p-GaAs type structure at room temperature. J. Nanoelectron. Optoelectron. **14**(8), 1126–1132 (2019). https://doi.org/10.1166/jno.2019.2623
9. İ Yücedağ, G. Ersöz, A. Gümüş, Ş Altındal, Dielectric properties and electric modulus of Au/PPy/n-Si (MPS) type Schottky barrier diodes (SBDS) as a function of frequency and applied bias voltage. Int. J. Mod. Phys. B **29**(13), 1550075 (2015). https://doi.org/10.1142/S0217979215500757
10. V. Rajagopal Reddy, C. Venkata Prasad, Surface chemical states, electrical and carrier transport properties of Au/ZrO2/n-GaN MIS junction with a high-k ZrO2 as an insulating layer. Mater. Sci. Eng. B **231**, 74–80 (2018)
11. A. Ghobadi, T.B. Kallaos, I.M. Karunarathne, D.M. Gamachchi, A.C. Meng, J.C. Mathai, S. Gangopadhyay, S. Guha, Engineered semiconductor-dielectric interfaces in polymer ferroelectric transistors. J. Mater. Chem. C **13**(26), 13454–13463 (2025). https://doi.org/10.1039/D5TC01378J
12. J. Pająk, M. Ziemski, B. Nowak, Poly (vinyl alcohol)-biodegradable vinyl material. Chemik **64**(7), 527–530 (2010)
13. N. Mittal, T.-M. Jang, S.-W. Hwang, M. Niederberger, PVA–$FeCl_3$ composites as substrate and packaging materials for the controlled degradation of non-degradable metals in transient electronics. J. Mater. Chem. A **11**(24), 12999–13006 (2023). https://doi.org/10.1039/D2TA09507F
14. S.M. Ansari, A. Younis, Y.D. Kolekar, C.V. Ramana, Cobalt ferrite nanoparticles: the physics, synthesis, properties, and applications. Appl. Phys. Rev. **12**(2), 21308 (2025). https://doi.org/10.1063/5.0244555
15. N. Yahya, M. Kashif, N. Nasir, M. Niaz Akhtar, N.M. Yusof, Cobalt ferrite nanoparticles: an innovative approach for enhanced oil recovery application. J. Nano Res. **17**, 115–126 (2012). https://doi.org/10.4028/www.scientific.net/JNanoR.17.115
16. Anchal, Sarita, N. Jakhar, P.A. Alvi, B.L. Choudhary, Comprehensive analysis of Cu-doped CoFe2O4 nanocrystals: Structural, morphological, optoelectronic, and magnetic properties. Adv. Powder Technol. **36**(1), 104748 (2025). https://doi.org/10.1016/j.apt.2024.104748
17. M. Basak, M.L. Rahman, M.F. Ahmed, B. Biswas, N. Sharmin, Calcination effect on structural, morphological and magnetic properties of nano-sized CoFe2O4 developed by a simple co-precipitation technique. Mater. Chem. Phys. **264**, 124442 (2021). https://doi.org/10.1016/j.matchemphys.2021.124442

18. Y. Kumar, A. Sharma, P.M. Shirage, Impact of different morphologies of CoFe2O4 nanoparticles for tuning of structural, optical and magnetic properties. J. Alloys Compd. **778**, 398–409 (2019). https://doi.org/10.1016/j.jallcom.2018.11.128
19. Y. Eom, M. Abbas, H. Noh, C. Kim, Morphology-controlled synthesis of highly crystalline Fe_3O_4 and $CoFe_2O_4$ nanoparticles using a facile thermal decomposition method. RSC Adv. **6**(19), 15861–15867 (2016). https://doi.org/10.1039/C5RA27649G
20. F. Rehman, H.-B. Jin, L. Wang, A. Tanver, D.-Z. Su, J.-B. Li, Effect of Nd^{3+} substitution for Bi^{3+} on the dielectric properties and conduction behavior of Aurivillius $NdBi_4Ti_3FeO_{15}$ ceramics. RSC Adv. **6**(25), 21254–21260 (2016). https://doi.org/10.1039/C5RA27821J
21. W.S. Mohamed, A.M. Abu-Dief, Impact of rare earth europium (RE-Eu3+) ions substitution on microstructural, optical and magnetic properties of CoFe2−xEuxO4 nanosystems. Ceram. Int. **46**(10), 16196–16209 (2020). https://doi.org/10.1016/j.ceramint.2020.03.175
22. S.B. Das, R.K. Singh, V. Kumar, N. Kumar, P. Singh, N. Kumar Naik, Structural, magnetic, optical and ferroelectric properties of Y^{3+} substituted cobalt ferrite nanomaterials prepared by a cost-effective sol-gel route. Mater. Sci. Semicond. Process. **145**, 106632 (2022). https://doi.org/10.1016/j.mssp.2022.106632
23. H.L. Andersen, M. Saura-Múzquiz, C. Granados-Miralles, E. Canévet, N. Lock, M. Christensen, Crystalline and magnetic structure–property relationship in spinel ferrite nanoparticles. Nanoscale **10**(31), 14902–14914 (2018). https://doi.org/10.1039/C8NR01534A
24. F. Rehman, J.-B. Li, P. Ahmad, Y. Saeed, H.-B. Jin, Dielectric relaxation and electrical properties of Na0.5Bi4La0.5Ti4O15 electroceramics. J. Electroceram. **44**(3–4), 147–153 (2020). https://doi.org/10.1007/s10832-020-00205-8
25. F. Rehman, J.-B. Li, Y. Saeed, P. Ahmad, Dielectric behaviors and electrical properties of Gd-doped Aurivillius KBi4Ti4O15 ceramics. J. Mater. Sci. Mater. Electron. **31**(17), 14674–14680 (2020). https://doi.org/10.1007/s10854-020-04030-1
26. M.A. Rafiq, A. Javed, M.N. Rasul, M.A. Khan, A. Hussain, Understanding the structural, electronic, magnetic and optical properties of spinel MFe_2O_4 (M = Mn, Co, Ni) ferrites. Ceram. Int. **46**(4), 4976–4983 (2020). https://doi.org/10.1016/j.ceramint.2019.10.237
27. X. Xie, B. Wang, Y. Wang, C. Ni, X. Sun, W. Du, Spinel structured MFe_2O_4 (M = Fe, Co, Ni, Mn, Zn) and their composites for microwave absorption: a review. Chem. Eng. J. **428**, 131160 (2022). https://doi.org/10.1016/j.cej.2021.131160
28. J. Ma, B. Zhao, H. Xiang, F.-Z. Dai, Y. Liu, R. Zhang, Y. Zhou, High-entropy spinel ferrites MFe_2O_4 (M = Mg, Mn, Fe Co, Ni, Cu, Zn) with tunable electromagnetic properties and strong microwave absorption. J. Adv. Ceram. **11**(5), 754–768 (2022). https://doi.org/10.1007/s40145-022-0569-3
29. N. Ambikeswari, S. Manivannan, Structural, magnetic, and dielectric properties of ultrafine nickel-substituted cobalt ferrite-reduced graphene oxide nanocomposites. J. Electron. Mater. **50**(11), 6135–6148 (2021). https://doi.org/10.1007/s11664-021-09130-0
30. H. Lu, C. Li, K. Chen, Q. He, F. Ren, J. Wu, R. Dai, Facile synthesis of $CoFe_2O_4$@SiO_2 nanoparticles anchored on reduced graphene oxide for highly efficient electromagnetic wave absorption. RSC Adv. **15**(32), 25872–25884 (2025). https://doi.org/10.1039/D5RA03579A
31. T.Y. Lee, Y.-J. Kim, S. Ahn, D.-Y. Jeon, Electrically tunable ideality factor and series resistance of gate-controlled graphene/pentacene Schottky junctions. IEEE J. Electron Devices Soc. **12**, 379–383 (2024). https://doi.org/10.1109/JEDS.2024.3397014
32. M.-M. Dong, Y.-H. Liu, C.-K. Wang, X.-X. Fu, First-principles study of gate-tunable reversible rectifying behavior in 2D WGe_2N_4–$TaSi_2N_4$ heterojunction diodes: implications for logic devices. ACS Appl. Nano Mater. **6**(19), 17464–17472 (2023). https://doi.org/10.1021/acsanm.3c02561
33. J.A. Cloninger, R. Harris, K.L. Haley, R.M. Sterbentz, T. Taniguchi, K. Watanabe, J.O. Island, A back-to-back diode model applied to van der Waals Schottky diodes. J. Phys. Condens. Matter **36**(45), 455301 (2024). https://doi.org/10.1088/1361-648X/ad69ef
34. N.A. Al-Ahmadi, Metal oxide semiconductor-based Schottky diodes: a review of recent advances. Mater. Res. Express. **7**(3), 032001 (2020). https://doi.org/10.1088/2053-1591/ab7a60
35. S. Li, J. Chen, X. He, Y. Zheng, C. Yu, H. Lu, Comparative study of the micro-mechanism of charge redistribution at metal-semiconductor and semimetal-semiconductor interfaces: Pt(Ni)-MoS_2 and Bi-MoS_2(WSe_2) as the prototype. Appl. Surf. Sci. **623**, 157036 (2023). https://doi.org/10.1016/j.apsusc.2023.157036
36. Shivani, A.G. Chakkar, P. Kumar, M. Kumar, Interface engineering for minimizing trapped charge density in β-Ga_2O_3 Schottky barrier diodes for high-performance power devices. Mater Today Phys **50**, 101605 (2025). https://doi.org/10.1016/j.mtphys.2024.101605

37. E. Yükseltürk, E. Tanrıkulu, Incorporation of chromium nanostructures into PVC interlayer to improve electrical features of Au/n-Si schottky diodes. Phys. Scr. **100**(1), 0159a8 (2025). https://doi.org/10.1088/1402-4896/ad9fb8
38. İ Taşçıoğlu, Y. Badali, S. Altındal Yerişkin, Enhanced electrical parameters of the Au/n-Si Schottky barrier diodes with graphite/graphane oxide doped PVC interlayer. Phys. Scr. **99**(8), 085950 (2024). https://doi.org/10.1088/1402-4896/ad5b9c
39. A. Feizollahi Vahid, S. Alptekin, N. Basman, M. Ulusoy, Y. Şafak Asar, Ş Altındal, The investigation of frequency dependent dielectric properties and ac conductivity by impedance spectroscopy in the Al/(Cu-doped diamond like carbon)/Au structures. J. Mater. Sci. Mater. Electron. **34**(13), 1118 (2023). https://doi.org/10.1007/s10854-023-10546-z
40. C.D. Pham, J. Chang, M.A. Zurbuchen, J.P. Chang, Magnetic properties of CoFe 2 O 4 thin films synthesized by radical-enhanced atomic layer deposition. ACS Appl. Mater. Interfaces **9**(42), 36980–36988 (2017). https://doi.org/10.1021/acsami.7b08097
41. P. Jing, J. Du, C. Jin, J. Wang, L. Pan, J. Li, Q. Liu, Improved coercivity and considerable saturation magnetization of cobalt ferrite (CoFe2O4) nanoribbons synthesized by electrospinning. J. Mater. Sci. **51**(2), 885–892 (2016). https://doi.org/10.1007/s10853-015-9416-z
42. R. Gholipur, Preparation and electromagnetic waves absorption performance of novel peanut shell/CoFe2O4/(RGO)x/PVA nanocomposites. Sci. Rep. **14**(1), 30699 (2024). https://doi.org/10.1038/s41598-024-79286-2
43. S.-Q. Su, S.-Q. Wu, S. Kanegawa, K. Yamamoto, O. Sato, Control of electronic polarization via charge ordering and electron transfer: electronic ferroelectrics and electronic pyroelectrics. Chem. Sci. **14**(39), 10631–10643 (2023). https://doi.org/10.1039/D3SC03432A
44. W.B. Fowler, Influence of electronic polarization on the optical properties of insulators. Phys. Rev. **151**(2), 657–667 (1966). https://doi.org/10.1103/PhysRev.151.657
45. S. Zhang, D. Lan, J. Zheng, Z. Zhao, Z. Jia, G. Wu, Insights into polarization relaxation of electromagnetic wave absorption. Cell Rep Phys Sci. **5**(9), 102206 (2024). https://doi.org/10.1016/j.xcrp.2024.102206
46. P.J.W. Debye, *Polar molecules* (Dover Publications, New York, 1929)
47. A. von Hippel, *Dielectrics and Waves* (Wiley, New York, 1954)
48. S. Siddabattuni, T.P. Schuman, F. Dogan, Dielectric properties of polymer-particle nanocomposites influenced by electronic nature of filler surfaces. ACS Appl. Mater. Interfaces **5**(6), 1917–1927 (2013). https://doi.org/10.1021/am3030239
49. C. Kittel, *Introduction to solid state physics*, 8th edn. (Wiley, New York, 2004)
50. V. Karagkiozaki, S. Logothetidis, A. Laskarakis, G. Giannoglou, S. Lousinian, AFM study of the thrombogenicity of carbon-based coatings for cardiovascular applications. Mater. Sci. Eng. B Adv. Funct. Solid-State Mater. **152**(1–3), 16–21 (2008). https://doi.org/10.1016/j.mseb.2008.06.013
51. R.H. Boyd, Relaxation processes in crystalline polymers: experimental behaviour — a review. Polymer (Guildf) **26**(3), 323–347 (1985). https://doi.org/10.1016/0032-3861(85)90192-2
52. G. Williams, D.C. Watts, Non-symmetrical dielectric relaxation behaviour arising from a simple empirical decay function. Trans. Faraday Soc. **66**, 80 (1970). https://doi.org/10.1039/tf9706600080
53. P. Liu, Z. Xie, X. Pang, T. Xu, S. Zhang, P.H.F. Morshuis, H. Li, Z. Peng, Space charge behavior in epoxy-based dielectrics: progress and perspective. Adv. Electron. Mater. **8**(10), 2200259 (2022). https://doi.org/10.1002/aelm.202200259
54. J.C. Maxwell, *A Treatise on Electricity and Magnetism* (Clarendon Press, 1873)
55. K.W. Wagner, Zur Theorie der unvollkommenen Dielektrika. Ann. Phys. **345**(5), 817–855 (1913). https://doi.org/10.1002/andp.19133450502
56. C.G. Koops, On the dispersion of resistivity and dielectric constant of some semiconductors at audiofrequencies. Phys. Rev. **83**(1), 121–124 (1951). https://doi.org/10.1103/PhysRev.83.121
57. K.L. Routray, D. Behera, Enhancement in conductivity and dielectric properties of rare-earth (Gd3+) substituted nano-sized CoFe2O4. J. Mater. Sci. Mater. Electron. **29**(16), 14248–14260 (2018). https://doi.org/10.1007/s10854-018-9558-2
58. J.-W. Xiao, B. Lin, G.-C. Bao, J.-M. Li, W.-K. Gu, F.-A. He, J.-S. Xu, K.-H. Lam, Improved properties of CoFe2O4@rGO/PVDF composites prepared through a solution-mixing approach. Diam. Relat. Mater. **146**, 111132 (2024). https://doi.org/10.1016/j.diamond.2024.111132
59. K.V. Sankar, R.K. Selvan, D. Meyrick, Electrochemical performances of CoFe 2 O 4 nanoparticles and a rGO based asymmetric supercapacitor. RSC Adv. **5**(121), 99959–99967 (2015). https://doi.org/10.1039/C5RA14938J
60. G.E. Demir, I. Yücedağ, S.A. Yerişkin, Characterization of surface states and their relaxation time in Al/ZnO/ p -GaAs structure by admittance method at room temperature. J.

Nanoelectron. Optoelectron. **14**(5), 653–659 (2019). https://doi.org/10.1166/jno.2019.2624

61. Y. Azizian-Kalandaragh, İ Yücedağ, G. Ersöz Demir, Ş Altındal, Investigation of the variation of dielectric properties by applying frequency and voltage to Al/(CdS-PVA)/p-Si structures. J. Mol. Struct. **1224**, 129325 (2021). https://doi.org/10.1016/j.molstruc.2020.129325
62. A. Baştuğ, I. Taşçıoğlu, A. Khalkhali, Ş Altındal, M. Yıldırım, S. Sarıtaş, Exploring the dielectric and AC transport characteristics of Au/(Sn:Fe2O3)/n-Si diodes using impedance spectroscopy over extended frequency and voltage intervals. J. Mater. Sci. Mater. Electron. **36**(28), 1822 (2025). https://doi.org/10.1007/s10854-025-15906-5
63. E. Balcı, A.F. Vahid, B. Avar, Ş Altındal, On a detail examination of frequency and voltage dependence of dielectric, electric modulus, ac conductivity (σ) of the Al/DLC/p-Si structures between 2 kHz and 1 MHz. Phys. B Condens. Matter **695**, 416576 (2024). https://doi.org/10.1016/j.physb.2024.416576
64. A. Barkhordari, H. Mashayekhi, P. Amiri, Ş Altındal, Y. Azizian-Kalandaragh, On the investigation of frequency-dependent dielectric features in Schottky barrier diodes (SBDs) with polymer interfacial layer doped by graphene and ZnTiO3 nanostructures. Appl. Phys. A **129**(4), 249 (2023). https://doi.org/10.1007/s00339-023-06539-8
65. Ç.Ş Güçlü, A. Khalkhali, S.A. Hameed, İ Taşçıoğlu, A. Demirci, Ş Altındal, Dielectric response of Au/(Co:PVA)/n-Si/Al structures under varying frequencies and bias voltages. J. Mater. Sci. Mater. Electron. **36**(23), 1431 (2025). https://doi.org/10.1007/s10854-025-15485-5
66. X. Geng, M. Vega-Paredes, Z. Wang, C. Ophus, P. Lu, Y. Ma, S. Zhang, C. Scheu, C.H. Liebscher, B. Gault, Grain boundary engineering for efficient and durable electrocatalysis. Nat. Commun. **15**(1), 8534 (2024). https://doi.org/10.1038/s41467-024-52919-w

Publisher's Note Springer Nature remains neutral with regard to jurisdictional claims in published maps and institutional affiliations.